



**HAL**  
open science

## Dense and nanometric electronic excitations induced by swift heavy ions in an ionic CaF<sub>2</sub> crystal: Evidence for two thresholds of damage creation

M. Toulemonde, A. Benyagoub, C. Trautmann, N. Khalfaoui, M. Boccanfuso, C. Dufour, F. Gourbilleau, J. Grob, J. P. Stoquert, J. M. Costantini, et al.

### ► To cite this version:

M. Toulemonde, A. Benyagoub, C. Trautmann, N. Khalfaoui, M. Boccanfuso, et al.. Dense and nanometric electronic excitations induced by swift heavy ions in an ionic CaF<sub>2</sub> crystal: Evidence for two thresholds of damage creation. *Physical Review B: Condensed Matter and Materials Physics* (1998-2015), 2012, 85 (5), pp.054112. 10.1103/PhysRevB.85.054112 . hal-00675130v1

**HAL Id: hal-00675130**

**<https://hal.science/hal-00675130v1>**

Submitted on 21 Jun 2018 (v1), last revised 1 Jun 2022 (v2)

**HAL** is a multi-disciplinary open access archive for the deposit and dissemination of scientific research documents, whether they are published or not. The documents may come from teaching and research institutions in France or abroad, or from public or private research centers.

L'archive ouverte pluridisciplinaire **HAL**, est destinée au dépôt et à la diffusion de documents scientifiques de niveau recherche, publiés ou non, émanant des établissements d'enseignement et de recherche français ou étrangers, des laboratoires publics ou privés.

# Dense and nanometric electronic excitations induced by swift heavy ions in an ionic CaF<sub>2</sub> crystal: Evidence for two thresholds of damage creation

M. Toulemonde,<sup>1,\*</sup> A. Benyagoub,<sup>1</sup> C. Trautmann,<sup>2</sup> N. Khalfaoui,<sup>1</sup> M. Boccanfuso,<sup>1</sup> C. Dufour,<sup>1</sup> F. Gourbilleau,<sup>1</sup> J. J. Grob,<sup>3</sup>  
J. P. Stoquert,<sup>3</sup> J. M. Costantini,<sup>4</sup> F. Haas,<sup>5</sup> E. Jacquet,<sup>1</sup> K.-O. Voss,<sup>2</sup> and A. Meftah<sup>6</sup>

<sup>1</sup>*CIRIL, Grand Accélérateur National d'Ions Lourds (GANIL), CEA-CNRS-ENSICAEN, BP 5133, Bd H. Becquerel, 14070 Caen, Cedex 5, France*

<sup>2</sup>*GSI Helmholtzzentrum für Schwerionenforschung, Planckstr. 1, 64291 Darmstadt, Germany*

<sup>3</sup>*INeSS, CNRS, Univ. Strasbourg, 23 rue du loess, 67037 Strasbourg, France*

<sup>4</sup>*CEA/SACLAY, DMN/SRMA, 91191 Gif sur Yvette, France*

<sup>5</sup>*IPHC, CNRS, Univ. Strasbourg, 23 rue du loess, 67037 Strasbourg, France*

<sup>6</sup>*LRPCSI, Université 20 août 1955-Skikda, route d'El-Hadaiek, BP 26, 21000 Skikda, Algeria*

CaF<sub>2</sub> crystals as representatives of the class of ionic nonamorphizable insulators were irradiated with many different swift heavy ions of energy above 0.5 MeV/u providing a broad range of electronic energy losses ( $S_e$ ). Beam-induced modifications were characterized by Channeling Rutherford Backscattering Spectrometry (C-RBS) and x-ray diffraction (XRD), complemented by transmission electron microscopy (TEM). Results from C-RBS give evidence of significant damage appearing above a  $S_e$  threshold of  $5 \pm 2$  keV/nm. A second critical  $S_e$  appears around  $18 \pm 3$  keV/nm; below this value the damage as function of ion fluence saturates at 20%, while above this the damage saturation level increases with  $S_e$ , reaching  $\sim 60\%$  for ions of  $S_e = 30$  keV/nm. XRD measurements also show effects indicating two threshold values. Above 5 keV/nm, the widths of the XRD reflection peaks increase due to the formation of nanograins, as seen by TEM, while a significant decrease of the peak areas only occurs above 18 keV/nm. The track radii deduced from C-RBS measurements are in agreement with those extracted from the fluence evolution of the widths of the XRD peaks. Moreover, track radii deduced from the peak area analysis are slightly smaller but in agreement with previous track observations by high resolution electron microscopy. Calculations based on the inelastic thermal spike model suggest that the lower threshold at 5 keV/nm is linked to the quenching of the molten phase, whereas the threshold at 18 keV/nm can be interpreted as quenching of the boiling phase. The results of CaF<sub>2</sub> are compared with other nonamorphizable materials such as LiF and UO<sub>2</sub>.

## I. INTRODUCTION

High-energy heavy ions, either as mass fragments from natural fission processes or as MeV-GeV projectiles delivered by large accelerator facilities, generate trails of excitations and ionizations along their paths. This energy initially deposited on the electrons finally dissipates in the crystal structure, and in many solids so-called ion tracks are formed. Ion tracks are denoted as 'latent tracks' because they are not visible by eye or optical microscopy due to their small diameters of only few nanometers. Nanotechnology with ion tracks is in most cases based on a selective etching process which dissolves the original track in a suitable chemical solvent converting the track into an open nano- or micrometer sized channel.<sup>1-7</sup> After the discovery of ion tracks in the late 1950s<sup>8</sup> until today, high resolution techniques in particular transmission electron microscopy (TEM) have been essential to directly image and characterize tracks with respect to their size and structure. Nowadays a large body of data is available for tracks in metallic,<sup>9-12</sup> semiconducting,<sup>13-20</sup> and most notably insulating materials.<sup>21-25</sup> The following paragraphs present a short overview of the present knowledge of track creation in amorphizable and nonamorphizable insulators and motivate the need of a comprehensive study on CaF<sub>2</sub>.

## A. Tracks in amorphizable insulators

Most investigations on amorphizable insulators<sup>26</sup> were performed in a regime of electronic energy loss ( $S_e$ ) where tracks are continuous amorphous cylinders embedded in a crystalline matrix. The interface to the surrounding crystal is rather sharp<sup>27</sup> and allows tracks to be easily revealed due to the high image contrast. For all materials studied so far, the track radius is only a few nanometers. Track formation requires a material-dependent critical energy loss. Above this threshold, the track size in a given material becomes larger with increasing energy loss. Close to the track formation threshold, Houpert *et al.*<sup>28</sup> showed that the track morphology changes from continuous to discontinuous, consisting of less-extended damage fragments (the effect has been ascribed to fluctuating energy loss processes,<sup>29</sup> but it has not yet been clarified). With decreasing energy loss, the fragments become shorter, and the diameter does not change but remains constant at around 2–3 nm. This observation is important because it tells us that an extrapolation of the track size versus electronic energy loss is not a suitable method for the determination of the track formation threshold.<sup>28,30</sup> Moreover, high-resolution TEM imaging and quantitative size analysis is difficult for discontinuous tracks.

In contrast to direct-track observation, several other techniques, including measurements of the order-to-disorder damage transformation,<sup>31</sup> volume swelling,<sup>32-35</sup> magnetic-to-

paramagnetic transition,<sup>29,36</sup> or electrical resistivity changes,<sup>37</sup> overcome this problem by measuring the overall track damage of a given sample. In such studies typically the damage cross section ( $\sigma$ ) is deduced by analyzing the amount of transformed material as a function of the ion fluence<sup>31–37</sup> and applying a Poisson statistical model that takes into account sublinear effects due to track overlapping.<sup>38</sup> The electronic energy loss threshold of track formation is determined by linear extrapolation of the cross section towards smaller  $S_e$ . The track radius  $R$  is deduced from the cross section assuming a continuous cylindrical track geometry with  $\sigma = \pi R^2$ . Since the cross section or  $R^2$  (Refs. 30 and 39–41), based on observations made on many materials, is linear with  $S_e$ , the radius should follow a square root law of  $S_e$ . This size analysis is an indirect method to extract track radii but so far gave good agreement with TEM observations as long as the radius of the track is larger than 2–3 nm.<sup>30</sup>

In various materials, ion tracks were intensively investigated by scanning force microscopy (SFM) showing in most cases little protrusions at the impact site of each ion projectile.<sup>42–49</sup> For mica, e.g., the radius of the protrusions<sup>46</sup> coincides well with the track radius deduced from other techniques<sup>24</sup> since the protrusions are negligible due to fresh cleaving or very little on a surface directly exposed to ion irradiation (in contrast to other materials, the height of the protrusions in mica are too small for quantitative size analysis<sup>47</sup>). The results obtained from several direct (TEM, SFM) and indirect [Mössbauer spectrometry, Channeling Rutherford Backscattering (C-RBS) and x-ray diffraction (XRD)] observation methods lead to a consistent determination of the  $S_e$  thresholds in various amorphizable insulators including mica,<sup>24,43,46,48,50,51</sup> yttrium iron garnet ( $\text{Y}_3\text{Fe}_5\text{O}_{12}$ ),<sup>52,53</sup> gadolinium gallium garnet ( $\text{Gd}_3\text{Ga}_5\text{O}_{12}$ ),<sup>54,55</sup> and crystalline quartz ( $\text{SiO}_2$ ).<sup>30,56</sup>

When comparing track sizes and  $S_e$  thresholds from different irradiation experiments, it is important to check if the velocities of the projectiles are similar.<sup>52,57</sup> The ion velocity determines the size of the radial dose distribution from the electron cascade. For a given energy loss, the deposited energy

density is larger at low ion velocity,<sup>58</sup> leading to a larger track radius than at high ion velocity.<sup>52</sup>

Based on the overall consistency of experimental track data, the inelastic thermal spike model has been developed to describe the track size and  $S_e$  threshold. This thermodynamic approach<sup>30,59</sup> takes into account the initial extension of the energy deposition on the electrons as well as the subsequent electron diffusion process. The energy is transferred to the atom subsystem via an electron-atom coupling. The model assumes that the track corresponds to the quenching of a molten phase, thus the amorphous track size is determined as a cylinder in which the energy density deposited on the atoms surpassed the energy necessary for melting. This approach has been extended to surface processes such as sputtering of particles by surface sublimation. For crystalline  $\text{SiO}_2$  as target, the experimental sputtering rate could be described with the same set of parameters as for the description of the track size in the bulk.<sup>60</sup>

## B. Tracks in nonamorphizable insulators

Although many experimental track data coincide quite well with thermal spike calculations, the present description is not yet coherent for materials that cannot be amorphized. Numerous experiments give clear evidence that tracks exist in various nonamorphizable materials including oxides and ionic crystals. The amorphization criterion seems to be directly linked to the strength of the ionic bonding, i.e., a larger ionicity degree renders materials less subjected to amorphization.<sup>61</sup> This applies for oxides such as  $\text{SnO}_2$ ,<sup>62–64</sup>  $\text{UO}_2$ ,<sup>65,66</sup> yttria-stabilized  $\text{ZrO}_2$ ,<sup>67,68</sup> zirconate pyrochlore  $\text{Gd}_2\text{Zr}_2\text{O}_7$ ,<sup>69</sup> and also to alkaline and alkaline earth halides.<sup>70–74</sup> All TEM observations show that tracks in these nonamorphizable crystals are smaller than in amorphizable oxides such as  $\text{Y}_3\text{Fe}_5\text{O}_{12}$ ,<sup>53</sup>  $\text{Gd}_3\text{Ga}_5\text{O}_{12}$  garnets,<sup>55</sup> crystalline  $\text{SiO}_2$ ,<sup>56</sup> and titanate pyrochlore  $\text{Gd}_2\text{Ti}_2\text{O}_7$ <sup>69</sup> [Fig. 1(a)]. In contrast, when using other characterization methods, e.g., C-RBS, the indirectly deduced size of tracks in yttria-stabilized  $\text{ZrO}_2$  is at least two times larger than the values obtained from

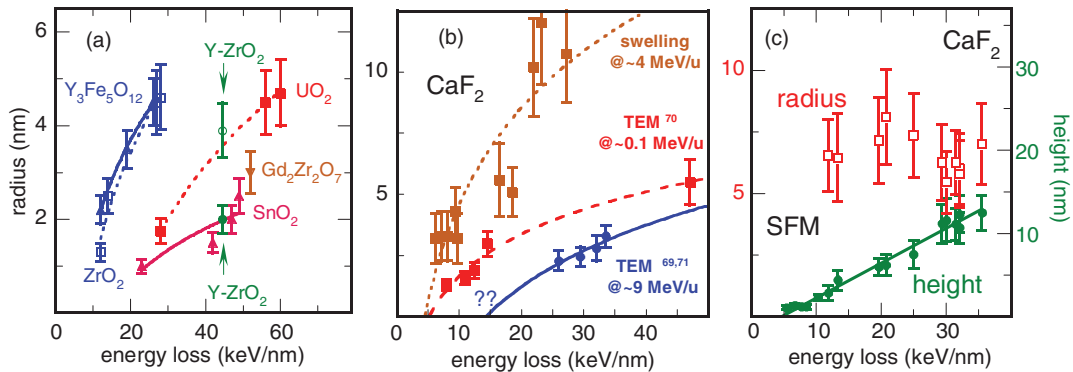


FIG. 1. (Color online) (a) Track radii in various oxide materials: TEM radii (full symbols) in nonamorphizable oxides [ $\text{UO}_2$ ,  $\text{Gd}_2\text{Zr}_2\text{O}_7$ ,  $\text{SnO}_2$ , yttria-stabilized zirconia ( $\text{Y-ZrO}_2$ )] are smaller than in amorphizable oxide ( $\text{Y}_3\text{Fe}_5\text{O}_{12}$ ). The track radii (open points) deduced from XRD analysis of pure  $\text{ZrO}_2$  and C-RBS analysis of  $\text{Y-ZrO}_2$  are larger than radii from direct observations by TEM. (b) Track radii in  $\text{CaF}_2$  irradiated with ions of specific energy around  $\sim 4$  MeV/u and with C60 projectiles of 0.1 MeV/u. Track radii deduced from swelling measurements (open circles) are larger than radii of surface hillocks [see (c)] and larger than TEM radii (full squares) independent of beam energy. (c) Radii and heights of surface hillocks in  $\text{CaF}_2$ . The extrapolation of the height data to the x-axis yields an electronic energy loss threshold equal to the value deduced from swelling measurements.

direct microscopic observations.<sup>67,68</sup> In pure  $\text{ZrO}_2$ , ion irradiation results in a transformation from the monoclinic to the tetragonal structure.<sup>75–78</sup> The cross section of this phase transformation as deduced by XRD yields similar large track radii as in amorphizable insulators [Fig. 1(a)]. Large cross sections are also observed in  $\text{Y}_2\text{O}_3$ , which undergoes a cubic-to-monoclinic phase transformation.<sup>79</sup> The obvious difference between direct microscopic track imaging and track sizes deduced indirectly, e.g., by XRD, raises the question of whether the sensitivity of a given observation technique may have an influence on the determination of the track size. As mentioned previously, the interface between the track and the surrounding crystal is rather sharp whenever the track consists of amorphous material<sup>27</sup> and the structural difference is characterized by a high contrast. However, in nonamorphizable oxides the track consists of a modified but still crystalline structure probably enriched with defects and defect clusters. Under such conditions, the track does not necessarily provide a good imaging contrast with respect to the surrounding intact matrix.

For nonamorphizable crystals, LiF can be regarded as a model system because it is a pure ionic compound and does not amorphize. Irradiation experiments with many different light and heavy ions revealed a complex damage morphology,<sup>33</sup> including point defects and defect clusters.<sup>70</sup> For LiF, track imaging by TEM is problematic because the electron beam decomposes the crystal readily. Also other analytical techniques using particle beams (e.g., C-RBS) may harm the structure and thus cannot be applied for reliable damage quantification.

### C. Track formation in $\text{CaF}_2$

To complement information on track formation in non-amorphizable ionic crystals, track appearance in calcium fluoride was investigated.  $\text{CaF}_2$  has also a strong ionic binding preventing amorphization. Its radiation resistance is slightly better than that of LiF, thus various methods for damage characterization can be applied. Analyzing tracks in  $\text{CaF}_2$  will help to better understand response to swift heavy ions and specific damage phenomena in other nonamorphizable crystals with the fluorite structure. This concerns, for instance,  $\text{UO}_2$ <sup>65,66</sup> (or  $\text{CeO}_2$  as a surrogate<sup>80–82</sup>), a nuclear material that has to withstand high dose radiation from fission fragments.

Track data for  $\text{CaF}_2$ <sup>72–74,83–88</sup> existing so far were obtained by different techniques, including direct and indirect observations. Observations by means of TEM reveal a complex track structure consisting of faceted and/or intermittent fragments.<sup>72–74</sup> Details of the damage could not be resolved due to quick degradation under the analyzing electron beam. For a given energy loss, the track radii for projectiles of low specific energy ( $\sim 0.1$  MeV/u<sup>73</sup>) are significantly larger than for ions of high specific energy ( $\sim 9$  MeV/u<sup>72,74</sup>), in agreement with the velocity effect discussed previously.<sup>52</sup> For  $\text{CaF}_2$ , ion-induced surface hillocks measured by SFM<sup>72,83</sup> have radii larger than those observed by TEM<sup>72–74</sup> [Figs. 1(b) and 1(c)], in contrast to amorphizable oxides like mica.<sup>24,46</sup> This discrepancy may originate from a different geometrical shape of the surface protrusions that can be rather flat (e.g., mica) or spherical in shape,<sup>89</sup> as observed by high resolution electron microscopy in non-amorphizable  $\text{Gd}_2\text{Zr}_2\text{O}_7$ .

Comparing TEM<sup>72–74</sup> and SFM results for surface hillocks<sup>72,83</sup> with indirect damage characterization by means of volume swelling<sup>34</sup> allows the following conclusions: (i) track-related swelling increases above a critical energy loss [Fig. 1(b)]; (ii) track radii deduced from SFM seem to be independent of  $S_e$  [Fig. 1(c)]; (iii) track sizes deduced from swelling and SFM are significantly larger than values deduced from TEM observations<sup>72–74</sup> [Figs. 1(b) and 1(c)]; and (iv) data available from TEM are too limited to provide information on the energy loss threshold. However, assuming that the track radius increases, the square root of  $S_e$  yields a threshold of about 15 keV/nm [continuous blue line in Fig. 1(b)].

To untangle the puzzle of the different track radii and damage threshold values in  $\text{CaF}_2$ , this paper presents additional experimental results on tracks in  $\text{CaF}_2$  analyzed by C-RBS,<sup>88</sup> XRD,<sup>51,90,91</sup> and TEM complementing earlier investigation by SFM, TEM, and profilometry mentioned previously. The new data may help to clarify the differences of tracks in amorphizable and nonamorphizable insulators.

Such investigations will also serve as a severe test for different thermal spike scenarios. The approach of Szenes<sup>92</sup> excluded the velocity effect<sup>52,54,93</sup> and assumed that tracks generated by cluster projectiles and observed by TEM<sup>73</sup> result from the quenching of a molten phase. In contrast, the approach of Toulemonde *et al.* takes into account the velocity effect<sup>59,72–74</sup> and supposes that ion tracks in  $\text{CaF}_2$  are a consequence of the quenching of a boiling phase. The present experiments also aim at shedding more light in this large discrepancy in data interpretation.

## II. EXPERIMENTAL

### A. Ion irradiation

All  $\text{CaF}_2$  samples were irradiated at room temperature under normal incidence with ion species ranging from  $^4\text{He}$  to  $^{238}\text{U}$  of specific energy between 0.5 and 13.7 MeV/u. The experiments were performed at different accelerators: the Medium Energy Line (“Sortie Moyenne Energie,” SME) at GANIL in Caen (France), the UNILAC (beamline X0) at GSI in Darmstadt (Germany), the 6-MV tandem in Bruyères le Chatel (France), the VIVITRON at the IPHC laboratory in Strasbourg (France), and the 4-MV single stage Van de Graaff at the INeSS Laboratory in Strasbourg (France). For homogeneous sample irradiation, the beam at the UNILAC was defocused by means of quadrupole magnets. All other facilities are equipped with a sweeping system allowing exposure of samples of at least  $2 \times 2$  cm<sup>2</sup>. Stripper foils mounted in front of the target provided ions of equilibrium charge state. Deviations from the known energy loss<sup>94</sup> at or just below the sample surface were thus avoided.<sup>95,96</sup> The stripper foils also served as an ion-flux monitor system by continuously recording the electrical current due to electron emission calibrated by a downstream Faraday cup.<sup>97</sup> The irradiation were performed at room temperature, and in order to minimize sample heating the ion flux was limited to values between  $3 \times 10^8$  and  $10^9$  ions/cm<sup>2</sup>/s, depending on the ion species. According to calculations, the flux of  $3 \times 10^8$  Pb/cm<sup>2</sup> of energy 4.6 MeV/u leads to an increase of temperature of less than 20 °C. The maximum applied fluence was selected

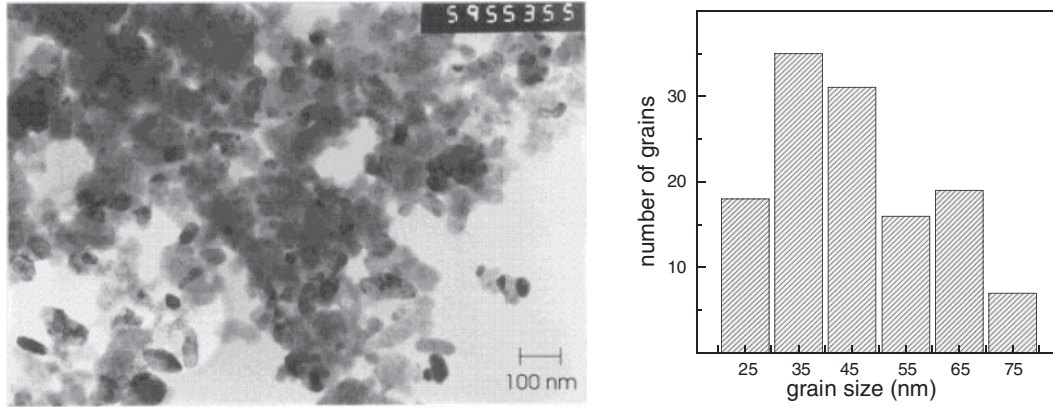


FIG. 2. TEM image of  $\text{CaF}_2$  grain powder before irradiation (left) and size distribution (right), yielding an average grain size of  $45 \pm 9$  nm.

according to the electronic energy loss and ranged from  $10^{12} \text{ cm}^{-2}$  for heavy ions to  $10^{17} \text{ cm}^{-2}$  for light ions. C-RBS experiments were performed on large single crystals of 10 mm in diameter. For XRD measurements, ultrapure  $\text{CaF}_2$  powder, provided by Merck, was pressed into 15-mm-diameter and 1.5-mm-thick pellets. The powder samples were inspected by TEM using a JEOL (200 CX) instrument operated at 200 keV (Fig. 2). The grain diameter of the virgin powder was 45 nm with a standard deviation of  $\pm 9$  nm.

A detailed list of the irradiation parameters is presented in Tables I and II for XRD and C-RBS experiments, respectively. The ion projected range ( $R_p$ ) and electronic energy loss ( $S_e$ ) were calculated with the computer code SRIM2003<sup>98</sup> with an estimated uncertainty of about 15%.

### B. X-ray diffraction (XRD)

Before ion irradiation and during beam stops, XRD spectra were collected using a standard spectrometer placed in the irradiation chamber of the SME beam line at GANIL. *In-situ* XRD analysis allowed us to avoid handling or repositioning of the samples between the different fluence steps. Quartz-monochromated  $\text{Cu-K}\alpha$  radiation was used in combination with a curved-position sensitive gas detector (CPS120 from INEL) covering diffraction angles ( $2\theta$ ) from 10 to  $130^\circ$ .<sup>99,100</sup>

The spectrometer was set up with a parafocused x-ray beam in a back reflection mode at a fixed incidence angle for a flat plate specimen. The sample was mounted on a holder that continuously rotated around the axis normal to the sample surface. A typical spectrum for virgin  $\text{CaF}_2$  is given in Fig. 3. The position, intensity, and width of each diffraction line were determined after deconvolution by a pseudo-Voigt function. The instrumental resolution, determined using a Si powder as a reference, and the XRD data of virgin  $\text{CaF}_2$  powder<sup>101</sup> are given in Table III.

The angle of x-ray beam incidence was  $12 \pm 2^\circ$  with respect to the sample surface. Under this condition, the crystals were probed within a thickness of about  $8 \pm 2 \mu\text{m}$ , which is significantly thinner than the projected range of the ions (cf., Table I). Moreover, due to the small tested layer thickness, the electronic energy loss can be regarded as nearly constant, and the nuclear energy loss does not contribute. The mean energy loss listed in Table I corresponds to the energy deposited by the ions within the probed layers.

During x-ray measurements, special care was taken to minimize signals from sample activation due to nuclear reactions. This effect is in particular crucial for irradiations with light ions such as Ar, Ni, and Kr and leads to irrelevant counts in the gas detector, which decrease the absolute counting rate by overloading the electronic data acquisition

TABLE I. Irradiation parameters and results from x-ray diffraction analysis of irradiated  $\text{CaF}_2$ . The irradiation facility is given in the column entitled acc. The electronic energy loss ( $S_e$ ) corresponds to the ion energy deposited in the x-ray probed sample layer. Initial slopes  $I$ , saturation value  $S$ , damage cross sections  $\sigma$ , and the track radii  $R$  are deduced from XRD data by analyzing the fluence evolution of the diffraction lines. Index  $a$  refers to the analysis of the peak area and index  $w$  to the analysis of the peak width. The minimum grain size  $g_{\text{min}}$  after irradiation to the highest fluence is deduced from the peak width using the Debye-scherrer formula (initial grain size according to XRD  $41 \pm 3$  nm).

Beam	acc	Energy MeV/u	Flux ions/cm <sup>2</sup> /s	Fluence ions/cm <sup>2</sup>	Range $\mu\text{m}$	Mean $S_e$ keV/nm	$I_a^a$ nm <sup>2</sup> /ion	$S_a$	$\sigma_a$ nm <sup>2</sup>	$R_a$ nm	$I_w$ nm <sup>2</sup> /ion	$1 + S_w$	$\sigma_w$ nm <sup>2</sup>	$R_w$ nm	$g_{\text{min}}$ nm
<sup>36</sup> Ar	GANIL	3.8	$10^9$	$8.5 \times 10^{13}$	27	5.5	<0.2	>0.98	<0.05	<0.1	1.9(8)	—	—	—	—
<sup>58</sup> Ni	GANIL	3.1	$5 \times 10^8$	$3 \times 10^{13}$	23	9.1	<0.3	>0.97	<0.2	<0.2	10(3)	1.58(5)	17(6)	2.3(7)	21(1)
<sup>78</sup> Kr	GANIL	3.6	$5 \times 10^8$	$2 \times 10^{13}$	27	13	<0.4	>0.96	<0.2	<0.2	50(15)	1.68(5)	60(20)	4.4(1.5)	19(1)
<sup>127</sup> I	Vivitron	1.6	$7 \times 10^8$	$7.9 \times 10^{13}$	18	16	<0.3	>0.96	<0.1	<0.18	34(12)	1.56(5)	57(20)	4.3(1.5)	21(1)
<sup>129</sup> Xe	GANIL	2.7	$6 \times 10^8$	$1.5 \times 10^{13}$	23	23	0.9(6)	<0.92	4.5(3.5) <sup>b</sup>	1.2(9) <sup>b</sup>	95(30)	1.92(6)	100(35)	5.6(1.8)	16(1)
<sup>208</sup> Pb	GANIL	4.1	$3 \times 10^8$	$0.6 \times 10^{13}$	37	32	6(2)	0.82(2)	35(10)	3.3(1.0)	330(70)	1.96(6)	320(110)	10(3)	15(1)

<sup>a</sup>Absolute values.

<sup>b</sup>Assuming  $S_a = 0.82$ , as deduced from the Pb irradiation.

TABLE II. Irradiation parameters and results from Channeling Rutherford backscattering analysis. The electronic energy loss ( $S_e$ ) corresponds to the value at the sample surface,  $I_d$  is the initial rate of the damage increase,  $S_d$  the relative value of the damage at saturation,  $\sigma_d$  the damage cross section, and  $R_d$  the damage radius deduced from cross section. (acc indicates the accelerator facility, with 6 MV standing for the tandem facility in Strasbourg.)

Beam	acc	Energy MeV/u	Flux Ions/cm <sup>2</sup> /s	Fluence ions/cm <sup>2</sup>	$S_e$ keV/nm	$I_d$ nm <sup>2</sup> /ion	$S_d$	$\sigma_d$ nm <sup>2</sup>	$R_d$ nm
<sup>4</sup> He	INeSS	0.5	10 <sup>12</sup>	10 <sup>17</sup>	0.4	<0.001	–	–	–
<sup>16</sup> O	GANIL	13.7	10 <sup>10</sup>	10 <sup>14</sup>	0.5	<0.02	–	–	–
<sup>32</sup> S	GANIL	11.2	10 <sup>9</sup>	10 <sup>14</sup>	1.6	<0.2	–	–	–
<sup>36</sup> Ar	GANIL	13.4	10 <sup>9</sup>	10 <sup>14</sup>	2.9	<0.6	–	–	–
	GANIL	6.3	10 <sup>9</sup>	10 <sup>14</sup>	4.2	<0.6	–	–	–
<sup>48</sup> Ca	GANIL	2.6	10 <sup>9</sup>	5 × 10 <sup>13</sup>	6.7	0.9 (2)	0.26 (3)	3.5 (1.0)	1.1 (4)
<sup>58</sup> Ni	GANIL	3.1	5 × 10 <sup>8</sup>	2 × 10 <sup>13</sup>	9.9	4.2 (3.4)	0.20 (3)	21 (7)	2.6 (9)
<sup>63</sup> Cu	6MV	1.0	10 <sup>9</sup>	8 × 10 <sup>13</sup>	11	7.7 (2.6)	0.25 (4)	31 (10)	3.1 (1.1)
<sup>76</sup> Ge	GANIL	8.0	5 × 10 <sup>8</sup>	2 × 10 <sup>13</sup>	8.5	5.6 (2.0)	–	–	–
	GANIL	3.8	5 × 10 <sup>8</sup>	2 × 10 <sup>13</sup>	11	4.9 (2.8)	–	–	–
<sup>84</sup> Kr	GANIL	9.7	5 × 10 <sup>8</sup>	10 <sup>13</sup>	10	2.5 (1.0)	–	–	–
	GANIL	4.3	5 × 10 <sup>8</sup>	10 <sup>13</sup>	13	8.8 (1.7)	–	–	–
<sup>129</sup> Xe	GSI	7.2	2 × 10 <sup>8</sup>	4 × 10 <sup>12</sup>	19	27 (10)	0.20 (4)	140 (40)	6.6 (1.0)
	GANIL	2.7	6 × 10 <sup>8</sup>	10 <sup>13</sup>	21	31 (10)	0.32 (5)	100 (30)	5.7 (9)
<sup>197</sup> Au	GSI	11.1	10 <sup>8</sup>	4 × 10 <sup>12</sup>	27	50 (12)	0.44 (7)	110 (15)	5.9 (8)
	GSI	5.4	10 <sup>8</sup>	4 × 10 <sup>12</sup>	29	27 (10)	–	–	–
	GSI	2.3	10 <sup>8</sup>	4 × 10 <sup>12</sup>	29	50 (15)	0.50 (4)	100 (15)	5.6 (8)
<sup>208</sup> Pb	GANIL	4.1	3 × 10 <sup>8</sup>	1.7 × 10 <sup>12</sup>	30	65 (15)	0.45 (3)	140 ± 20	6.7 (7)
	GANIL	1.8	3 × 10 <sup>8</sup>	1.7 × 10 <sup>12</sup>	29	60 (9)	0.57 (5)	110 (20)	5.9 (1.0)
<sup>209</sup> Bi	GSI	9.0	10 <sup>8</sup>	10 <sup>12</sup>	29	66 (19)	0.44 (7)	140 (40)	6.7 (1.0)
<sup>238</sup> U	GSI	3.6	10 <sup>8</sup>	0.9 × 10 <sup>12</sup>	36	120 (40)	0.69 (12) <sup>a</sup>	190 (60) <sup>a</sup>	7.8 (1.5) <sup>a</sup>

<sup>a</sup>From extrapolation of  $S_d$  values versus  $S_e$ .

system. The x-ray measurements after each irradiation step were therefore delayed by a deactivation time between 30 and 60 minutes.

Under ion beam exposure, the originally white CaF<sub>2</sub> pellets became homogeneously brown. During the irradiation experiment, the surface of the samples was continuously monitored by video camera in order to identify disintegrations of irradiated brown surface grains that may generate virgin surface regions falsifying the results.

In contrast to the experiments performed at the GANIL facility, samples irradiated at the VIVITRON in Strasbourg

were analyzed by *ex-situ* XRD. Diffraction patterns were recorded under different angles of x-ray incidence between 2 and 24° with respect to the sample surface.

### C. Channeling Rutherford Backscattering Spectrometry (C-RBS)

Most samples for C-RBS experiments were prepared by cleaving thin platelets from a single crystal block of high purity calcium fluoride. Some samples were directly purchased (Korth Kristalle GmbH) as small slabs of single crystal of optical quality. The surface of the (100)-oriented samples had typical dimensions of  $\sim 10 \times 10 \times 1$  mm<sup>3</sup>. To improve the crystallinity near the surface, the platelets were annealed before ion irradiation at 400 °C in inert atmosphere for one hour.

During ion irradiation the samples were partially masked by a 500- $\mu$ m-thick aluminum foil with a clear-cut edge. The foil thickness is sufficiently thick to stop the ion beam and thus provided a virgin sample area in direct neighborhood to the bombarded area. Before the C-RBS analysis, the ion-irradiated samples were covered by a thin evaporated film of Pd ( $\sim 8$  nm) to avoid surface charging by the analyzing <sup>4</sup>He beam. The analysis of the radiation damage by C-RBS was performed with 2-MeV <sup>4</sup>He<sup>+</sup> ions (intensity  $\sim 3$ nA) at the 4 MV Van de Graaff accelerator of the INeSS laboratory in Strasbourg. The backscattered <sup>4</sup>He particles were detected in a silicon detector placed at 150° with respect to the incident beam with a solid angle of  $2.5 \times 10^{-3}$  steradians.

In order to minimize the damage by the analyzing <sup>4</sup>He beam (spot size  $\sim 1$  mm<sup>2</sup>), the total number of incident particles was limited to  $\sim 5 \times 10^{13}$ , corresponding to a fluence of

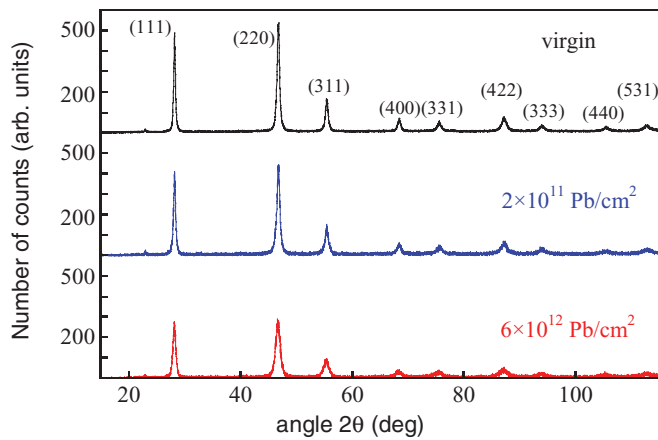


FIG. 3. (Color online) X-ray diffraction pattern of CaF<sub>2</sub> powder samples before and after irradiation with 4.1-MeV/u Pb ions at two different fluences.

TABLE III. XRD data of virgin  $\text{CaF}_2$  powder under x-ray beam incidence of  $12^\circ$  with respect to the sample surface. The intensities are normalized to the intensity of the (220) reflection.

$\text{CaF}_2$ index	(111)	(220)	(311)	(400)	(331)	(422)	(333)	(440)	(531)
Angle $2\theta$ ( $^\circ$ )	28.3	47.1	55.9	68.9	76.1	87.7	94.6	106.2	113.6
Theoretical intensity (%), Ref. 101	92	100	33	10	9	17	7	4	6
Experimental intensity (%)	62	100	31	13	12	24	10	9	13
Width ( $10^{-2}$ rad) for $\sim 41$ -nm $\text{CaF}_2$ grains	0.65	0.94	1.02	1.19	1.5	1.76	1.89	2.09	2.62
Width ( $10^{-2}$ rad) intrinsic resolution	0.26	0.38	0.44	0.47	0.61	0.77	0.8	0.89	1.15

$5 \times 10^{15} \text{ cm}^{-2}$ , which is negligible as compared to the fluence needed to induce damage in  $\text{CaF}_2$ .<sup>88</sup> After sample alignment along the (111) direction on the virgin part, the sample was translated to the irradiated part. By a quick angular scan, it was verified that the aligned spectrum is recorded at minimum backscattering yield. For samples exposed to large fluences, this procedure appeared to be important because macroscopic swelling<sup>34</sup> leads to curved samples accompanied by a slight misalignment from optimum channeling conditions. It was also checked that during the C-RBS analysis time, the damage from the swift ion irradiation does not change due to the analyzing He beam.

### III. DATA ANALYSIS AND EXPERIMENTAL RESULTS

#### A. Analysis of XRD data

The XRD patterns before and after irradiation of fluorite with 4.1-MeV/u Pb ions at two low fluences are displayed in Fig. 3. None of the ion irradiations induce new peaks, but the peak intensities of all diffraction lines decrease and their peak width becomes larger with increasing fluence. Figure 4 shows the evolution of the peak of the strongest diffraction lines (111), (220), and (311) with ion fluence. Simultaneously, the positions of all peaks shift with increasing fluence go to lower angles. This effect is observed for all beams except for I ions, for which the strongest diffraction lines were analyzed *ex-situ* for different angles of the incident x-ray beam. After the irradiation with I ions, the peak intensities (Fig. 5) do not differ from those of the virgin sample, while the peak widths increase. This finding fixes the lower limit of the  $S_e$  threshold, as discussed further below.

For a quantitative analysis, the areas of the diffraction lines were normalized to the respective initial area of the nonirradiated sample. The normalized areas of the most

prominent diffraction lines (111), (220), and (311) plotted versus the ion fluence show a very similar trend [Fig. 6(a)]. This indicates that the irradiation did not induce a specific grain orientation (texture), as observed at very high fluences for NiO.<sup>102</sup> For further analysis, we thus averaged the normalized areas of these three peaks [Fig. 6(b)] and fitted an exponential curve based on a Poisson law:<sup>38</sup>

$$A(\Phi t) = (1 - S_a) \times \exp(-\sigma_a \times \Phi t) + S_a, \quad (1)$$

where  $A$  is the normalized peak area at a given fluence  $\Phi t$ ,  $S_a$  is the saturation value of  $A$  at high fluences ( $\Phi t \rightarrow \infty$ ), and  $\sigma_a$  is the damage cross section. The initial slope  $I_a = -\sigma_a \times (1 - S_a)$  describes the linear regime of nonoverlapping tracks and provides information on the track radius (assuming cylindrical track geometry) by  $\sigma_a = \pi \times R_a^2$ . The corresponding values ( $I_a$ ,  $S_a$ ,  $\sigma_a$ ) of all irradiation experiments are reported in Table I.

Figure 7 compiles the mean area decrease as a function of fluence for irradiations with Pb, Xe, and I ions. A decrease of the area of the diffraction peaks is only observed for irradiations with projectiles heavier than iodine corresponding to an electronic energy loss above 16 keV/nm.

Concomitant with decreasing peak area, the widths of the reflection lines increase as a function of ion fluence [Fig. 8(a)]. Comparing the normalized peak width (normalized to the corresponding value of the nonirradiated samples) shows that the different reflection lines evolve in a similar manner [Fig. 8(b)]. We thus deduced the averaged width of the most dominant peaks at a given fluence and use the mean value for further analysis. Figure 9 shows the mean width data for different heavy ions. Irradiations with ions lighter than Ar did not result in peak broadening. Applying an exponential fit (solid line in Fig. 9), the evolution of the XRD peak width

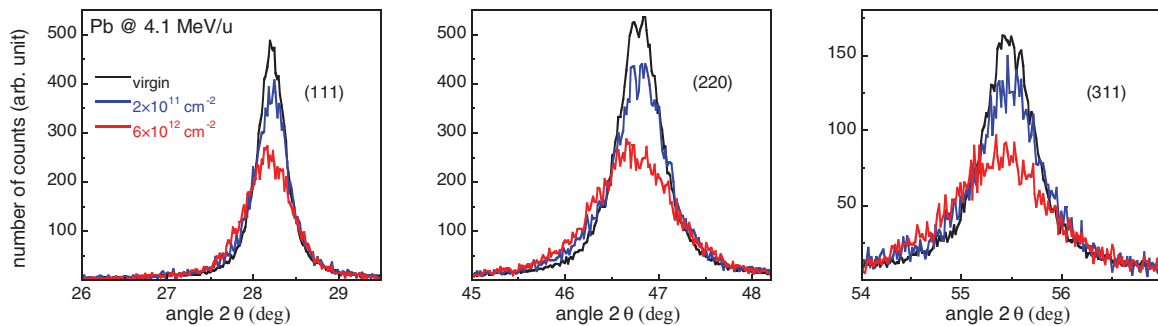


FIG. 4. (Color online) Enlarged view of diffraction lines (111), (220), and (311) before and after irradiation with 4.1-MeV/u Pb ions at low and high fluence.

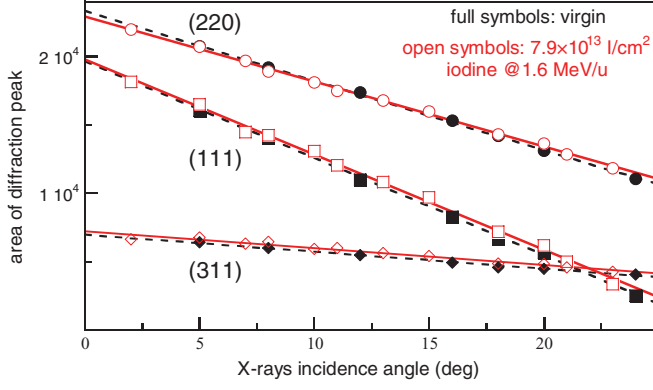


FIG. 5. (Color online) *Ex-situ* analysis of samples irradiated with I ions. Evolution of the area of three different diffraction peaks as a function of the angle of x-ray incidence (with respect to sample surface) for a CaF<sub>2</sub> pellet before (black full symbols, dashed line) and after irradiation with 1.6-MeV/u iodine ions (red open symbols, solid line). The lines are guides to the eye.

versus fluence is described by

$$W(\Phi t) = S_w \times (1 - \exp(-\sigma_w \times \Phi t)) + 1, \quad (2)$$

with  $\sigma_w$  being the cross section of the width increase. ( $S_w + 1$ ) is the maximum value of the normalized width for  $\Phi t \rightarrow \infty$ . The initial slope  $I_w$  of the width increase is equal to

$$I_w = \sigma_w \times S_w. \quad (3)$$

All values deduced for  $I_w$ ,  $(1 + S_w)$ , and  $\sigma_w$  are reported in Table I.

The widths of the diffraction peaks are more than two times larger than the instrumental resolution (cf. Table III), indicating that the CaF<sub>2</sub> powder consists of nanometric grains. The grain size was deduced from the analysis of the width of the XRD peaks after corrections for the  $K_\alpha$  doublet and instrumental broadening. Using the Debye-Scherrer analysis,<sup>100,103</sup> the initial size of the grains was  $41 \pm 3$  nm, quite in agreement with the TEM observation (Fig. 2). The increase of the peak width with ion fluence can be ascribed to grain fragmentation. This conclusion is supported by Fig. 10 presenting TEM images from the same sample area before and after irradiation with Pb ions at the fluence of  $2 \times 10^{12}$  ions/cm<sup>2</sup> and showing clear

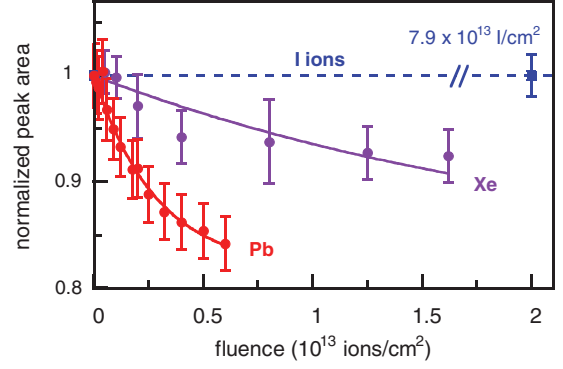


FIG. 7. (Color online) Normalized area [mean value of the reflection peaks (111), (220), and (311)] as a function of the fluence for the irradiations with 4.1-MeV/u Pb, 2.7-MeV/u Xe, and 1.6-MeV/u I ions. The lines are exponential fits based on a Poisson law [Eq. (1); Ref. 38], except for the iodine irradiation.

evidence of fragmentation of the initial grains. The grain size, as deduced by the Debye-Scherrer analysis, decreases with increasing ion fluence and finally reaches a minimum saturation value (Table I). The larger the electronic energy loss of the ion projectiles, the smaller is the final size of the produced nanograins.

## B. Damage analysis from C-RBS experiments

A typical set of Rutherford backscattering spectra of an irradiated and virgin crystal in random orientation and in channeling conditions along the (111) direction is shown in Fig. 11(a). Using a computer code developed by Hervé *et al.*,<sup>104</sup> the random spectrum was successfully simulated with  $3 \times 10^{13}$  <sup>4</sup>He particles, providing confidence in the measured <sup>4</sup>He flux during the C-RBS analysis. Moreover, the intensity of the Pd peak remained constant for the different samples [Fig. 11(a)], indicating that the measured <sup>4</sup>He fluence was steady whatever is the analyzed sample. Applying the surface approximation, the backscattering yield  $\chi$  was determined by extrapolating the backscattering yield of <sup>4</sup>He particles over

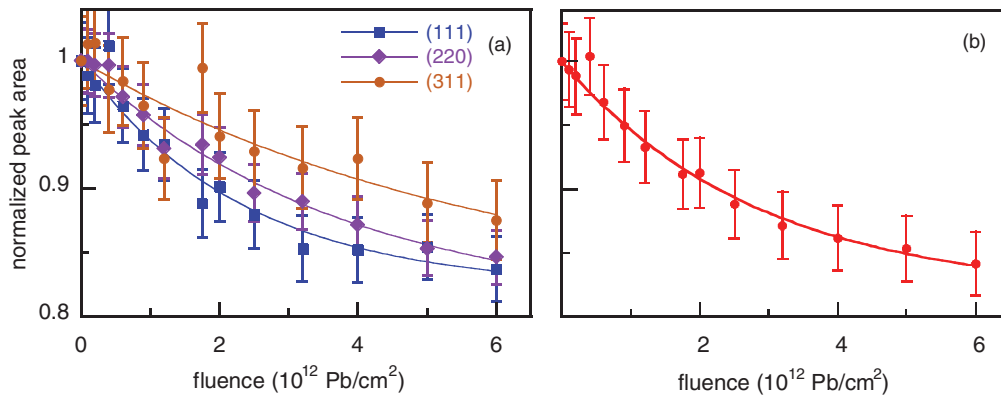


FIG. 6. (Color online) (a) Normalized area of the (111), (220), and (311) reflection peaks as a function of the fluence for the irradiation with 4.1-MeV/u Pb ions. (b) Averaged data of the three diffraction lines shown in (a). The lines are exponential fits based on a Poisson law [Eq. (1); Ref. 38].



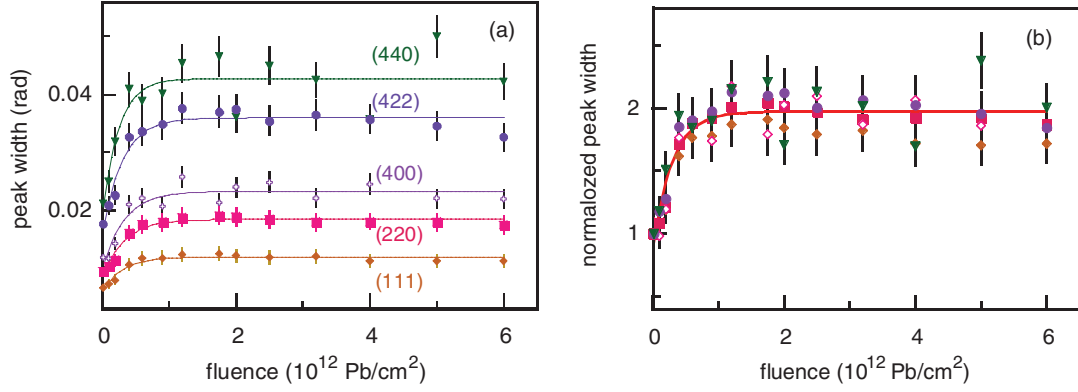


FIG. 8. (Color online) (a) Width of selected reflection peaks (111), (220), (400), (422), and (440) as a function of fluence for the irradiation with 4.1-MeV/u Pb ions. (b) Averaged data of normalized widths of diffraction lines shown in (a). The lines are exponential fits based on a Poisson law [Eq. (2); Ref. 38].

$\sim 300$  nm beyond the surface peak. The damage fraction  $D(\Phi t)$  was calculated according to

$$D(\Phi t) = (\chi_i(\Phi t) - \chi_v)/(\chi_r - \chi_v), \quad (4)$$

where  $\chi_i(\Phi t)$  and  $\chi_v$  denote the minimum backscattering yields under channeling condition of the irradiated part of the sample at a fluence  $\Phi t$  and the virgin part, respectively.  $\chi_r$  is the yield of the randomly oriented crystal and corresponds to a mean value of the irradiated and virgin part of the sample. The obtained damage fraction is plotted versus fluence for different incident heavy ions in Fig. 11(b). The evolution of the damage data can be described by the following exponential law:

$$D(\Phi t) = S_d \times (1 - \exp(-\sigma_d \times \Phi t)), \quad (5)$$

where  $\sigma_d$  is the cross section for damage creation and  $S_d$  is the maximum damage at high fluences ( $\Phi t \rightarrow \infty$ ). The initial slope of damage  $I_d$  is given by

$$I_d = \sigma_d \times S_d. \quad (6)$$

All values for  $I_d$ ,  $S_d$ , and  $\sigma_d$  are reported in Table II.

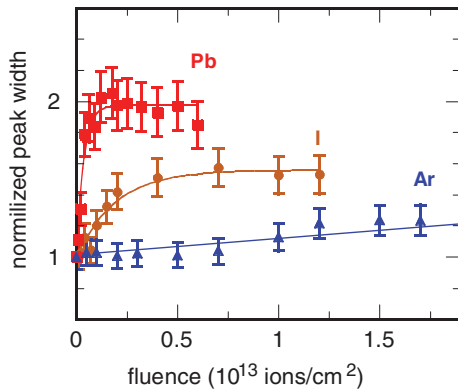


FIG. 9. (Color online) Evolution of width of reflection peaks as a function of fluence for the irradiations with 4.1-MeV/u Pb, 1.6-MeV/u I, and 3.8-MeV/u Ar ions. Width data were normalized to those of the pristine sample and averaged over the most intense XRD peaks. The lines are exponential fits based on a Poisson law [Eq. (2); Ref. 38].

### C. Discussion of experimental results

When comparing the initial rate of the damage increase per ion (i.e., nonoverlapping tracks) deduced from the different analytical methods (Fig. 12), we observe that the qualitative evolution of the initial slope of the widths of the XRD peaks ( $I_w$ ) is similar to the C-RBS data ( $I_d$ ). Both appear at the same electronic energy loss threshold, while the slope of the XRD peak area ( $I_a$ ) requires larger  $S_e$  values. The initial slope of the increase of the width and the decrease of the mean area deduced from XRD measurements [Fig. 12(a)] and the C-RBS damage [Fig. 12(b)] all follow a quadratic law with  $S_e$ , similar to the observation for swelling.<sup>34</sup>

Based on the different observations, the overall evolution of ion-induced damage in  $\text{CaF}_2$  can be summarized by the following characteristics.

(1) In the entire electronic energy-loss range presently studied, point defects are created apparent by the blue coloration of ion-irradiated crystals.<sup>84</sup> Below a threshold of  $5 \pm 2$  keV/nm, the damage measured by C-RBS and the width increase observed by XRD (Table II) are very small even at large fluences.

(2) For electronic energy losses above  $5 \pm 2$  keV/nm, damage is observed by C-RBS, which saturates at  $\sim 20\%$  at high fluences. It is correlated to the width increase of the XRD peaks linked to grain fragmentation [Fig. 13(a)]. This critical energy loss is in good agreement with the threshold observed for swelling<sup>34</sup> or when characterizing hillock appearance at the surface generated by individual ion impacts<sup>72,83</sup> [Figs. 1(b) and 1(c)].

(3) Above an electronic energy-loss threshold of  $\sim 18 \pm 3$  keV/nm, the diffraction peak area decreases and the damage at saturation (C-RBS data) increases with a continuation of the grain size decrease [Fig. 13(a)].

The cross sections for both width and damage increase are plotted in Fig. 13(b) versus the electronic energy loss showing a rather similar behavior within experimental errors. This result suggests that there is a strong correlation between the damage observed by C-RBS and the formation of nanograins.

Assuming cylindrical track geometry, track radii can be deduced from the damage cross section  $\sigma$  obtained from the C-RBS damage data and from the evolution of the area and width

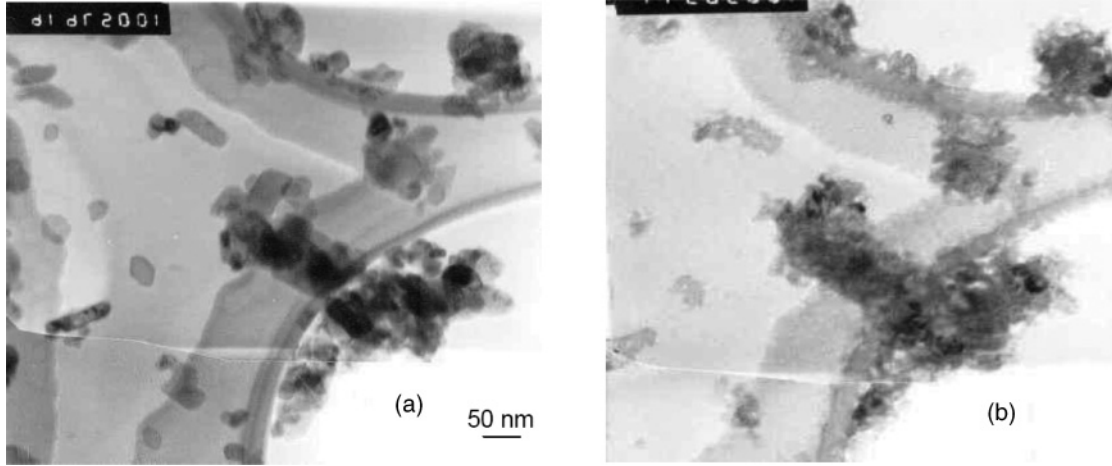


FIG. 10. TEM images of the same sample spot of  $\text{CaF}_2$  powder taken (a) before and (b) after irradiation with 4.1-MeV/u Pb ions of fluence  $10^{12}$  ions/cm<sup>2</sup>.

of the XRD peaks using  $\sigma = \pi R^2$ . The respective radii  $R_d$ ,  $R_a$ , and  $R_w$  are reported in Tables I and II. As expected from the cross-section comparison [Fig. 13(b)],  $R_d$  values coincide within the experimental errors with  $R_w$  values. It should be mentioned that radii deduced from the initial decrease of the XRD peak area agree well with track radii observed by TEM at 9 MeV/u.<sup>72,74</sup> Below 2.5 nm, where damage may become discontinuous,<sup>28,30</sup> the size of these radii corresponds to that of an effective radius, i.e., of a continuous cylindrical track having the same damage cross section.

#### IV. COMPARISON WITH INELASTIC THERMAL SPIKE MODEL

##### A. The inelastic thermal spike model

The inelastic thermal spike model (i-TS model)<sup>30,54,59,105</sup> was developed to describe and predict track radii in the electronic energy-loss regime. Based on heat transport equations,

it calculates how the energy initially deposited on the target electrons diffuses within the electron subsystem and is finally transferred to the atoms. The model was successfully applied for tracks in metals and numerous insulators.<sup>54,59</sup> The two differential equations that govern heat diffusion in time  $t$  and space  $r$  (radial distance from the ion path) in the electronic and atomic subsystems are coupled by the electron-phonon coupling constant  $g$ . Assuming a cylindrical geometry, the equations are solved numerically:<sup>106</sup>

$$C_e(T_e) \frac{\partial T_e}{\partial t} = \frac{1}{r} \frac{\partial}{\partial r} \left[ r K_e(T_e) \frac{\partial T_e}{\partial r} \right] - g(T_e - T_a) + A(r[v], t) \quad (7)$$

$$C_a(T_a) \frac{\partial T_a}{\partial t} = \frac{1}{r} \frac{\partial}{\partial r} \left[ r K_a(T_a) \frac{\partial T_a}{\partial r} \right] + g(T_e - T_a), \quad (8)$$

where  $T_{e,a}$ ,  $C_{e,a}$ , and  $K_{e,a}$  are the respective temperature, specific heat, and thermal conductivity of the electronic

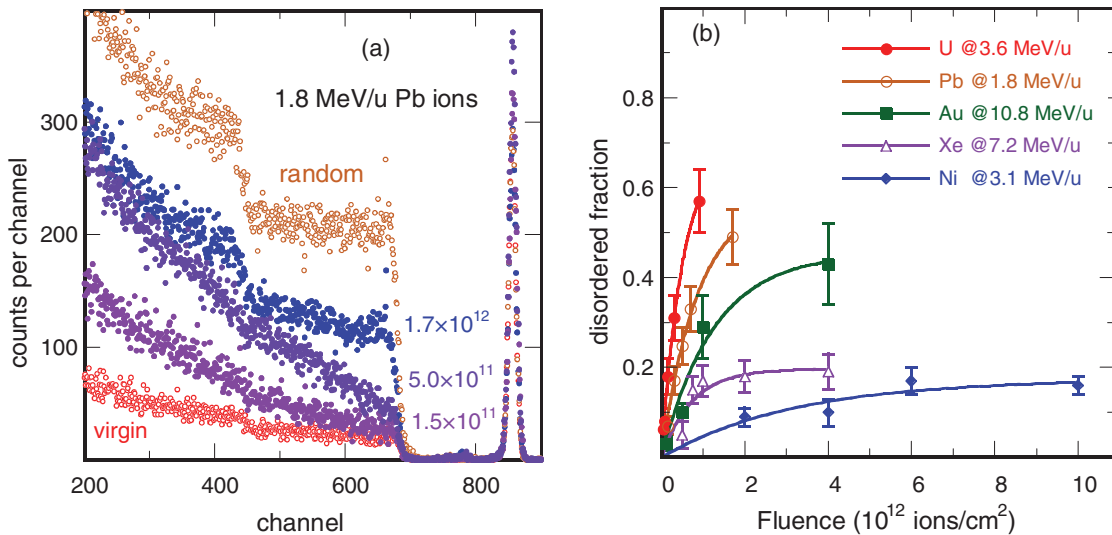


FIG. 11. (Color online) (a) C-RBS spectra of  $\text{CaF}_2$  irradiated with 1.8-MeV/u Pb ions (full symbols) compared to virgin sample under channeling (along [111] axis) and random condition (open symbols). The fluence is given in units of ions per cm<sup>2</sup>. (b) Damage fraction deduced from C-RBS experiments as a function of fluence for different ion beams. Solid lines are exponential fits using a Poisson law [Eq. (5); Ref. 38].

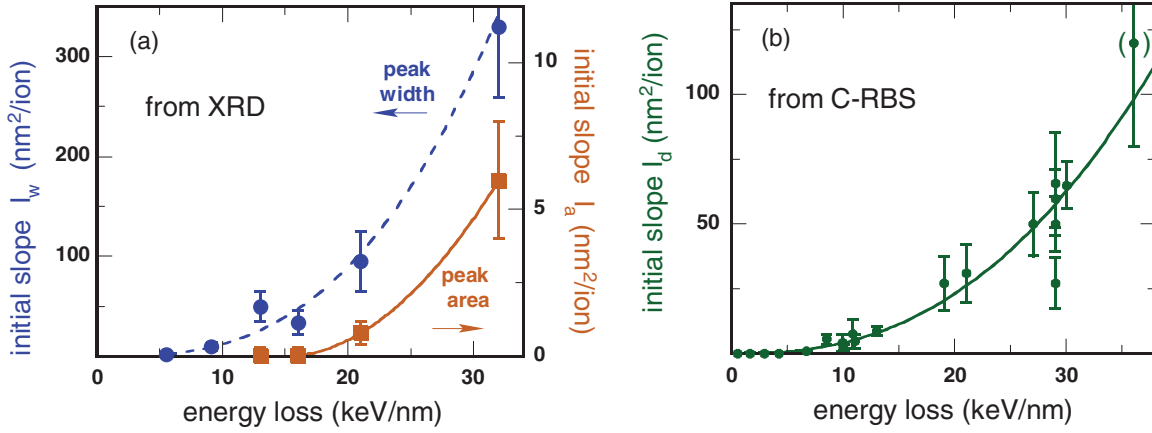


FIG. 12. (Color online) (a) Initial slope of normalized width increase ( $I_w$ ) and absolute  $I_a$  values of normalized peak area decrease from XRD peaks as a function of electronic energy loss. (b) Initial slope of the damage ( $I_d$ ) deduced from C-RBS data versus electronic energy loss.

and atomic subsystem. The values of the thermodynamical parameters of the atomic system are given in Table IV, while the values of the electronic subsystem are assumed to be constant.<sup>59</sup> The evolution of the different parameters of the material as a function of temperature is considered. The initial  $\sim 1/r^2$  energy distribution deposited on the target electrons ( $A(r[v], t)$ ) is taken into account. The ion-velocity dependant extension of the electron cascade is determined numerically by means of Monte-Carlo calculation.<sup>107</sup> When integrating  $A(r[v], t)$  over time and space, the deposited energy is equal to the corresponding electronic energy loss.

### B. Application of the inelastic thermal spike model to CaF<sub>2</sub>

Figure 14(a) shows the energy distribution in the electron subsystem for two different ion velocities (specific energies) in CaF<sub>2</sub>. We define a cylinder radius  $\alpha$  in which 66% of initial energy is deposited. For a given material,  $\alpha$  follows approximately the square root of the specific energy, and consequently it evolves linearly with ion velocity [Fig. 14(b)].<sup>30</sup>

Within the thermal spike code, the electron-phonon coupling  $g$  is the only free parameter. In the case of insulators,  $g$  is linked to the electron-phonon mean-free path  $\lambda$ <sup>59</sup> by

the relation  $\lambda^2 = A/g$  (with  $A = 2$  J/s/cm/K) and to the electron-phonon mean-free time by  $\tau = B/g$  (with  $B = 1$  J/cm<sup>3</sup>/K,) defining the respective mean length and mean time of the energy diffusion within the electron system before the energy is transferred to the lattice. Track data collected for a large number of different amorphizable materials suggests that the  $\lambda$  value is directly linked to the optical band gap<sup>54,59</sup> following a monotonic decrease, as expected.<sup>108</sup>

According to this, CaF<sub>2</sub> with a band gap<sup>109</sup> of 12 eV has a  $\lambda$  value<sup>59</sup> of 3.8 nm. Figure 14(b) compares the electron-phonon mean-free path  $\lambda$  with the cylinder radius  $\alpha$ , in which the initial energy is deposited on the electrons. If  $\lambda \gg \alpha$ ,  $\lambda$  defines the volume in which the energy is transferred from the electrons to the atoms, while for  $\lambda \ll \alpha$ , the energy transfer is governed by  $\alpha$ . In the intermediate range, both lengths have to be taken into account by a quadratic convolution<sup>30</sup> of  $\lambda$  and  $\alpha$ . The radius  $R_{\lambda+\alpha}$  in which the electronic energy loss is given to the atoms is then

$$R_{\lambda+\alpha}^2 = \lambda^2 + \alpha^2. \quad (9)$$

The effect of the ion velocity is in fact a phenomenon related to the deposited energy density that can be taken into account

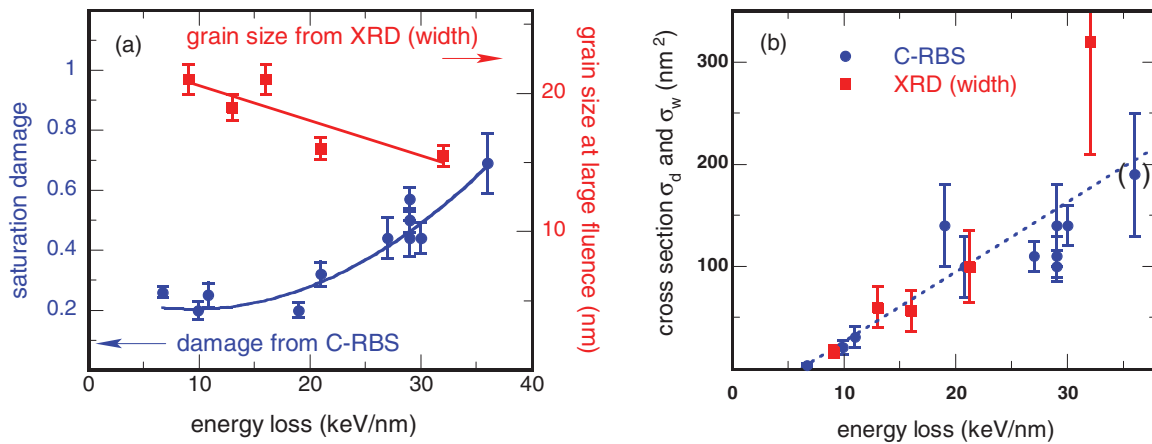


FIG. 13. (Color online) (a) Grain size at saturation versus electronic energy loss deduced from XRD measurements (red squares) and damage (blue circles) at saturation deduced from C-RBS measurements (lines are guides to the eyes). (b) Cross sections of width increase and damage increase versus fluence. The dotted red line is a linear fit to all data.

TABLE IV. Thermodynamic parameters for CaF<sub>2</sub>.

Thermal conductivity (J/K/cm/s)	0.05
Specific heat (J/g/K) >300 K	0.93
1500 K	1.58
Melting temperature (K)	1696
Latent heat of fusion (J/g)	220
Boiling temperature (K)	2773
Latent heat of vaporization (J/g)	2200
Density (g/cm <sup>3</sup> ) solid	3.18
Liquid	3.10

in a first approximation by considering  $R_{\lambda+\alpha}$ , the electronic excitation radius relevant for the energy transfer to the atoms.<sup>30</sup> Within this cylinder volume, the mean deposited energy per atom ( $E_{\text{at}}$ ) is equal to

$$E_{\text{at}} = S_e / (\pi \times R_{\lambda+\alpha}^2 \times N_{\text{at}}), \quad (10)$$

where  $N_{\text{at}}$  is the atomic density of CaF<sub>2</sub> and  $S_e$  the electronic energy loss at the corresponding beam energy. Track radii observed by TEM<sup>72–74</sup> and track radii deduced from the cross section of the initial decrease of the XRD peak area plotted versus  $E_{\text{at}}$  scatter around the same curve [Fig. 14(c)]. It shows in a first approximation that the energy density is the relevant parameter for explaining the velocity effect. Moreover, the energy necessary to create a track observed by TEM is around  $1.7 \pm 0.3$  eV/at, as deduced from the iodine irradiation for which  $R = 0$  (Table I).

As demonstrated for SnO<sub>2</sub> nanocrystals,<sup>63</sup> the grain size has to be considered in the thermal spike calculations only for a size below 35 nm. Such calculations are supported by experimental results where the sputtering rate of 35-nm nanograins of LiF<sup>110</sup> is quite in agreement with the bulk sputtering rate.<sup>111</sup> For our CaF<sub>2</sub> samples (grain size 45 nm), the sample is thus modeled as bulk material (infinite medium). Numerical calculations with the thermal spike model provide the evolution of the energy deposited on the atoms as a function of time and space (radial distance from ion path) within superheating scenario.<sup>60,111</sup> Results of the model using  $\lambda = 3.8$  nm are given in Fig. 15 for a

fixed electronic energy loss of 25 keV/nm, calculated for two different ion velocities. As for all other materials,<sup>59</sup> we applied the melting criterion for track formation by considering also the latent heat of melting  $E_m = 0.58$  eV/at of CaF<sub>2</sub>. This yields track radii of 7 nm for beam energy of 0.1 MeV/u and 5.2 nm for 10 MeV/u (Fig. 15). These values are much larger than track radii observed by TEM [Fig. 16(b)]. To test an alternative scenario which might be suitable for nonamorphizable crystals such as CaF<sub>2</sub>, the calculations were performed assuming that temperatures above the boiling phase are needed for track formation (see Fig. 6 in Ref. 59). The energy defining track formation is then the energy  $E_b$  to boil the material.  $E_b$  is composed of the melting energy  $E_m$  plus the energy to surpass the boiling temperature including the latent heat of boiling. The literature value for CaF<sub>2</sub> is  $E_b = 1.58$  eV/at. Plotting available TEM radius data as a function of the deposited number of eV/at [Fig. 14(c)] yields an experimental threshold of  $1.7 \pm 0.3$  eV/at, which is in quite good agreement with the literature value of  $E_b$ . For calculations with an energy loss of 25 keV/nm (Fig. 15), the track radii corresponding to the appearance of the boiling phase are 3.1 nm for 0.1 MeV/u and 1.6 nm for 10 MeV/u, and they are in agreement with the track radii observed by TEM [Fig. 16(a)]. The calculations were extended to a large range of electronic energy losses, and the evolution of the calculated radii versus  $S_e$  is plotted in Fig. 16(a) for two beam velocities. The overall agreement between our calculations and the experimental track radii supports the “boiling” scenario, yielding a good description of the track radii observed by TEM for low and high-velocity projectiles, contrary to the Szenes model.<sup>92</sup>

Using the melting criterion ( $E_m$ ) and the adopted  $\lambda$  value of 3.8 nm, the calculated tracks’ radii are in good agreement with  $\sim 4$  MeV/u ion irradiations, and track values deduced from C-RBS and XRD (increase of peak width) ascribed to grain fragmentation [Fig. 16(b)]. Moreover, calculations performed at very low velocity<sup>112</sup> [Fig. 16(a)] using the melting criterion predicts that the  $S_e$  threshold of damage creation in CaF<sub>2</sub> is around 1.7 keV/nm, a  $S_e$  value reached with an Ar beam of around 0.05 MeV/u (or 2 MeV).

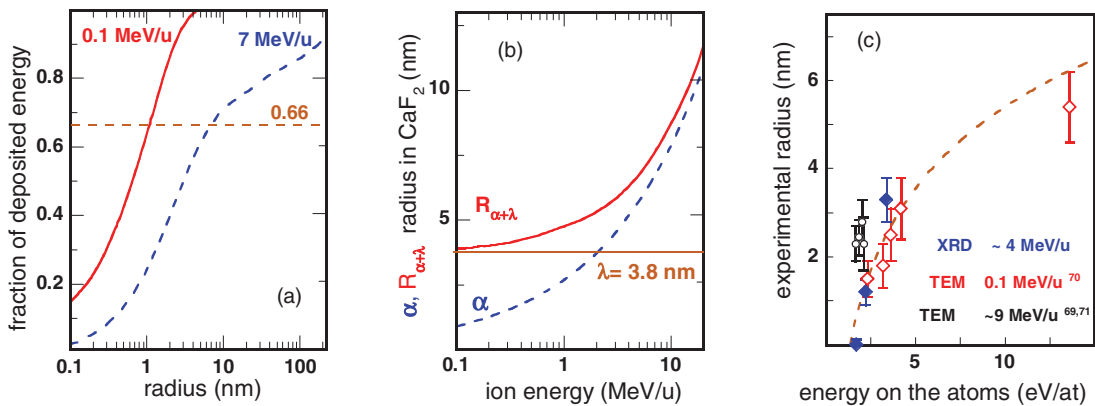


FIG. 14. (Color online) (a) Fraction of deposited energy versus radial distance from the ion trajectory calculated with the analytical formula from Waligorski *et al.* (Ref. 107)  $\alpha$  defines a cylinder radius in which 66% of the energy is deposited. (b) Cylinder radius  $\alpha$ , electron-phonon mean-free path  $\lambda = 3.8$  nm deduced for CaF<sub>2</sub>, and radius  $R_{\alpha+\lambda}$  obtained by convoluting  $\alpha$  and  $\lambda$  [Eq. (9)] plotted versus beam energy. (c) Track radii versus the deposited energy density (energy per atom) deduced with Eq. (10) from TEM observations and XRD measurements (initial decrease of peak area).

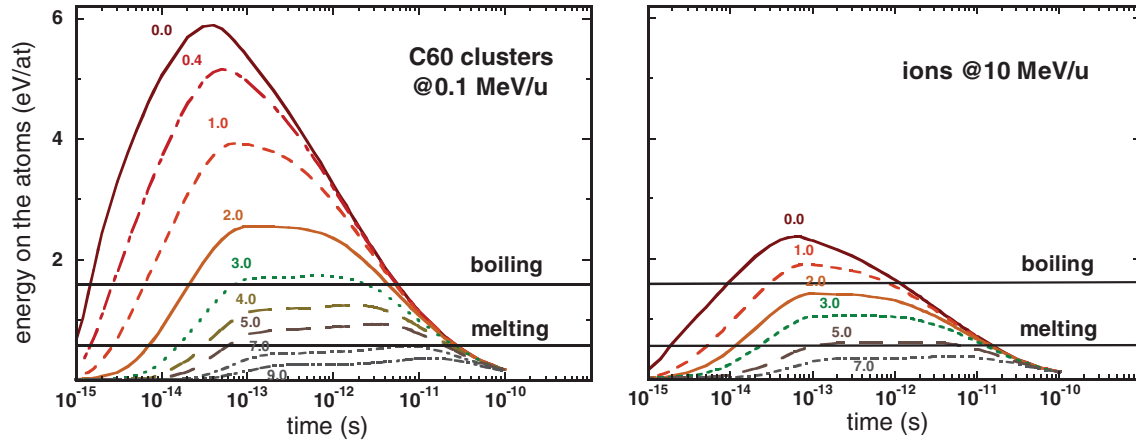


FIG. 15. (Color online) Thermal spike calculations for  $\text{CaF}_2$  irradiated with low-velocity C60 cluster projectiles and with high-velocity monoatomic ions. In both cases the electronic energy loss is 25 keV/nm. The lines show the energy deposited on the lattice atoms as a function of time at different radial distances from the projectile trajectory. The horizontal lines indicate the energy necessary for melting and boiling, both including latent heat.

### C. Correlation with other nonamorphizable crystals

The appearance of two thresholds in  $\text{CaF}_2$  supports the previous interpretation for tracks in  $\text{LiF}$ ,<sup>113</sup> where the melting and vaporization criteria were applied: swelling,<sup>32</sup> hillock formation,<sup>83</sup> and ultra-violet optical defects<sup>114</sup> above a critical  $S_e$  value of 3.5 keV/nm are ascribed to the appearance of a molten phase ( $E_m = 0.27$  eV/at), whereas the observation of tracks above a threshold of  $S_e \sim 14$  keV/nm measured by small angle x-ray scattering<sup>113,115,116</sup> was linked to a boiling phase ( $E_b = 1.27$  eV/at) (see Fig. 11 in Ref. 113). For additional confirmation,  $\text{LiF}$  powder was irradiated and XRD analyzed under very similar experimental conditions as  $\text{CaF}_2$ , using 4.1-MeV/u Pb and 7.3-MeV/u Kr ions of 22 and 11 keV/nm electronic energy loss, respectively. The widths of the XRD

peaks increased for both irradiations while the area decrease occurred only with Pb ions. These results were also correlated within the inelastic thermal spike model to the appearance of a molten phase above  $S_e = 3.5$  keV/nm and a boiling phase above  $S_e = 14$  keV/nm.<sup>113</sup> Extrapolations of the inelastic thermal spike model calculations to low ion energies yield for a beam of  $\sim 0.03$  MeV/u to a threshold of 1.6 keV/nm for the molten phase and 4.8 keV/nm for the boiling phase.

Another nonamorphizable material of interest is  $\text{UO}_2$ , which also has a fluorite structure. As a nuclear fuel material,  $\text{UO}_2$  is exposed to radiation with fission fragments. The knowledge of radiation-induced micro- and macrostructural changes is crucial concerning the durability of this material. Therefore, several previous experiments characterized ion

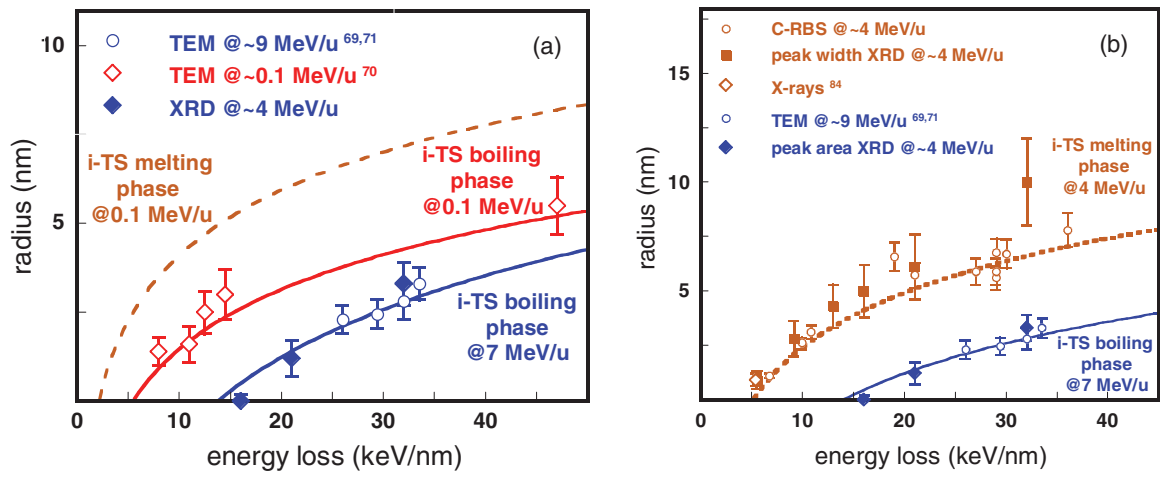


FIG. 16. (Color online) (a) Track radii in  $\text{CaF}_2$  observed by TEM versus electronic energy loss for irradiations with C60 projectiles (Ref. 73) at 0.1 MeV/u and for ions (Refs. 72 and 74) at 9 MeV/u. The track radii deduced from XRD measurements (initial decrease of peak area) using ions of  $\sim 7$  MeV/u are compared to TEM observations. Solid lines along experimental track data correspond to i-TS model calculations using the boiling energy as criterion and two different specific energies. The dashed line corresponds to calculations assuming quenching of the molten phase for cluster projectiles at 0.1 MeV/u. (b) Track radii versus electronic energy loss in  $\text{CaF}_2$  using ion beams in the  $\sim 6$  MeV/u energy range. Track sizes deduced from C-RBS data and from the XRD-peak width follow the same trend with a threshold around 5 keV/nm. The dashed line corresponds to thermal spike calculations using the melting criterion. Track radii observed by TEM and deduced from the XRD-peak area are plotted for comparison. The solid line corresponds to calculations using the boiling criterion as in (a).

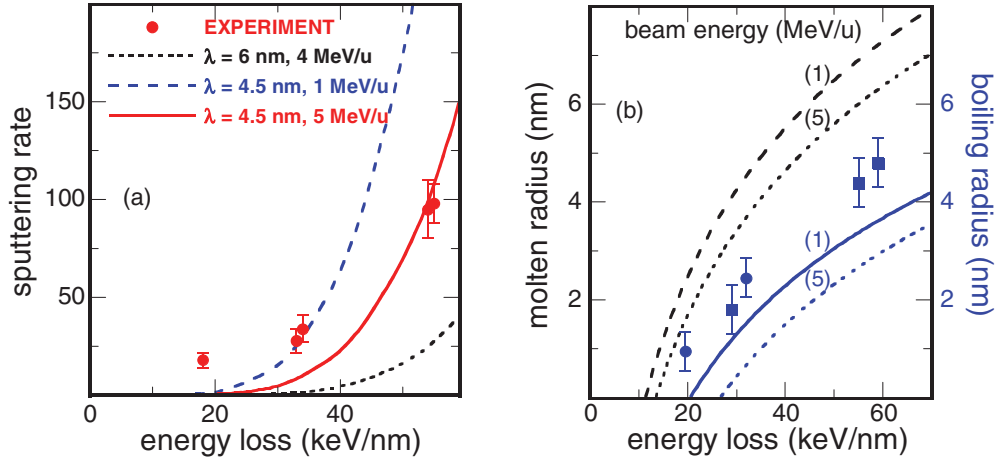


FIG. 17. (Color online) (a) Sputtering rate versus electronic energy loss for UO<sub>2</sub>. The lines correspond to the i-TS calculations using a sublimation energy of 2.68 eV/at and different values of  $\lambda$ . (b) Track radii versus electronic energy loss in UO<sub>2</sub>. The lines are calculations with  $\lambda = 4.5$  nm for 1 and 5 MeV/u. The upper two lines (black) correspond to the melting criterion and the lower two lines (blue) to the boiling criterion.

tracks in UO<sub>2</sub>. Track radii observed by TEM are of a similar size as tracks in CaF<sub>2</sub> (Fig. 1). Also sputtering yields<sup>117</sup> were measured by the collector technique. Sputtering yields and track data were calculated within the framework of the inelastic thermal spike model<sup>65</sup> using  $\lambda = 6$  nm deduced from the localized 5f electrons in the band gap,<sup>118,119</sup> which needs only 2 eV to reach the conduction band. The results are reported in Fig. 17(a) using a vaporization energy of 2.68 eV/at and the known thermodynamical parameters.<sup>65,120</sup> The calculated sputtering rate [Fig. 17(a)] is significantly lower than the experimental data,<sup>117</sup> putting some doubt on the previous description.<sup>65</sup> In contrast, using the optical band gap energy of 5 eV (Ref. 121), which corresponds to the *p-d* band gap and a  $\lambda$  value of 4.5 nm (Ref. 59), new calculations provide much better agreement with experimental sputtering rates within the beam energies investigated [Fig. 17(a)]. Recent molecular dynamics calculations can also reproduce the sputtering rate if the energy deposited on the electrons is transferred to the lattice atoms via an electron-phonon mean-free path of the order of 4 nm<sup>122</sup> supporting the present thermal spike calculations. Figure 17(b) shows experimental track sizes in UO<sub>2</sub><sup>65,66,80</sup> together with

calculated values (lines) using either the criterion of boiling ( $E_b = 2.68$  eV/at) or melting ( $E_m = 1.31$  eV/at). None of the criteria is able to reproduce the evolution of the track size with increasing energy loss, indicating either a lack in the inelastic thermal spike description or experimental limitations when determining the track size from TEM data. Despite these discrepancies, we extrapolated the model calculations to a beam energy of 0.5 MeV/u corresponding to fission fragment energy and found an electronic energy-loss threshold of  $\sim 11$  keV/nm when using the melting criterion. For fission fragments, the electronic energy loss in UO<sub>2</sub> is  $\sim 16$  keV/nm, and the damage cross section, calculated with the inelastic thermal spike model assuming melting is of the order of  $2 \times 10^{-14}$  cm<sup>2</sup>. For application of UO<sub>2</sub>, it should be considered that this value is significant larger than the cross section due to elastic collisions.<sup>123</sup>

## V. CONCLUSION

The damage induced by the irradiation with swift heavy ions was studied in CaF<sub>2</sub> by using different characterization techniques including XRD, channeling Rutherford backscattering, and TEM. These observations are complementing previous investigations by means of surface profilometry to measure swelling,<sup>34</sup> atomic force microscopy<sup>72,83</sup> to observe surface hillocks, high resolution electron microscopy to determine track diameters,<sup>72-74</sup> and optical absorption spectroscopy to quantify the creation of color centers.<sup>85</sup>

Compiling the large data set, we found evidence that specific phenomena appear above two different electronic energy-loss threshold values corresponding to two regimes of damage creation: (i) above  $S_e \sim 5 \pm 2$  keV/nm swelling appears, surface hillocks are formed, C-RBS reveals surface damage, and fragmentation into nanograins occurs; (ii) above  $\sim 18 \pm 3$  keV/nm tracks are visualized by TEM and the areas of XRD peaks decrease significantly with increasing ion fluence. Within the experimental uncertainties, the track radii extracted from the different physical characterizations coincide within the two threshold groups. This strongly suggests a track structure composed of different shells, as

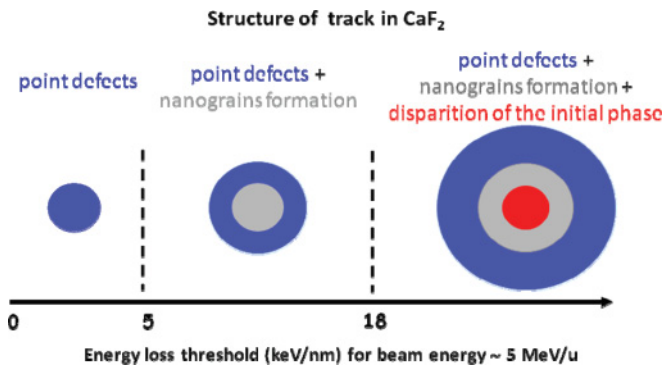


FIG. 18. (Color online) Scheme of shell-like track structure in CaF<sub>2</sub> for different ranges of energy losses. The defined range of energy losses varies with the beam energy: for a beam energy of 0.02 MeV/u the respective values of energy loss are 1.7 keV/nm and 5 keV/nm instead of 5 and 18 keV/nm.

sketched in Fig. 18, where the existence of the different shells is assigned to a specific range of electronic energy loss. Tracks with a core-shell structure were observed earlier for  $Y_3Fe_5O_{12}$ ,<sup>53</sup> LiF,<sup>113</sup> vitreous  $SiO_2$ ,<sup>124</sup> and pyrochlores,<sup>69</sup> but the assignment of the energy loss thresholds was not very clear.

Experimental track data in  $CaF_2$  were compared with inelastic thermal spike calculations. Using an electron-phonon mean-free path value equal to 3.8 nm (Ref. 59), small tracks produced above  $\sim 18 \pm 3$  keV/nm were assigned to tracks formed by quenching of a boiling phase, while larger track radii observed above  $\sim 5 \pm 2$  keV/nm were associated with the quenching of a molten cylinder. The agreement in the description of the different track shells in  $CaF_2$  suggests a general correlation of the electron-phonon coupling with

the optical band gap energy.<sup>54,59</sup> Moreover such a core-shell structure was predicted by molecular dynamics calculations<sup>125</sup> as a possible track description in  $CaF_2$ . These results improve the understanding of track formation but may also shed light on processes induced by high electronic excitation from femto-second laser pulses.<sup>126</sup>

Regarding other nonamorphizable oxides insulators such as  $SnO_2$ , it was shown that tracks observed by TEM are well described by thermal spike calculations assuming quenching of a boiling phase.<sup>63</sup> Applying such a description for  $UO_2$ , it was possible to reproduce qualitatively experimental sputtering yields. Based on the overall consistent description, our calculations predict that fission fragments of electronic energy loss below 20 keV/nm may induce damage in  $UO_2$ .

\*toulemonde@ganil.fr; <http://cimap.ensicaen.fr/>

- <sup>1</sup>R. L. Fleischer, P. B. Price, R. M. Walker, and E. L. Hubbard, *Phys. Rev.* **133**, 1443 (1964).
- <sup>2</sup>B. E. Fischer and R. Spohr, *Rev. Mod. Phys.* **55**, 907 (1983).
- <sup>3</sup>R. Spohr, in *Ion Tracks and Microtechnology, Basic Principles and Applications*, edited by K. Bethge (Vieweg, Germany, 1990).
- <sup>4</sup>D. A. Young, *Nature* **182**, 375 (1958).
- <sup>5</sup>C. Trautmann, W. Bröchle, R. Spohr, J. Vetter, and N. Angert, *Nucl. Instr. Meth. B* **111**, 70 (1993).
- <sup>6</sup>M. Skupinski, M. Toulemonde, M. Lindeberg, and K. Hjort, *Nucl. Instr. Meth. B* **240**, 681 (2005).
- <sup>7</sup>C. Trautmann, M. Toulemonde, C. Dufour, and E. Paumier, *Nucl. Instr. Meth. B* **108**, 94 (1996).
- <sup>8</sup>E. C. H. Silk and R. S. Barnes, *Philos. Mag.* **4**, 970 (1959).
- <sup>9</sup>A. Barbu, A. Dunlop, D. Lesueur, and R. S. Averback, *Europhys. Lett.* **15**, 37 (1991).
- <sup>10</sup>A. Dunlop, G. Jaskierowicz, P. M. Ossi, and S. Della-Negra, *Phys. Rev.* **76**, 155403 (2007).
- <sup>11</sup>V. Hardy, D. Groult, M. Hervieu, J. Provost, B. Raveau, and S. Bouffard, *Nucl. Instr. Meth. B* **54**, 472 (1991).
- <sup>12</sup>M. Leghissa, T. Schuster, W. Gerhauser, S. Klaumünzer, M. R. Koblichka, H. Kronmüller, H. Kuhn, H. W. Neumüller, and G. Saemann Ischenko, *Euro. Phys. Lett.* **19**, 323 (1992).
- <sup>13</sup>M. Toulemonde, J. Dural, G. Nouet, P. Mary, J. F. Hamet, M. F. Beaufort, J. C. Desoyer, C. Blanchard, and J. Auleytner, *Phys. Status Solidi A* **114**, 467 (1989).
- <sup>14</sup>A. Dunlop, G. Jaskierowicz, and S. Della-Negra, *Nucl. Instr. Meth. B* **146**, 302 (1998).
- <sup>15</sup>B. Canut, N. Bonardi, S. M. M. Ramos, and S. Della Negra, *Nucl. Instr. Meth. B* **146**, 296 (1998).
- <sup>16</sup>P. I. Gaiduk, A. N. Larsen, C. Trautmann, and M. Toulemonde, *Phys. Rev. B* **66**, 045316 (2002).
- <sup>17</sup>A. Colder, O. Marty, B. Canut, M. Levalois, P. Marie, X. Portier, S. M. M. Ramos, and M. Toulemonde, *Nucl. Instr. Meth. B* **174**, 491 (2001).
- <sup>18</sup>W. Wesch, A. Kamarou, E. Wendler, K. Gärtner, P. I. Gaiduk, and S. Klaumünzer, *Nucl. Instr. Meth. B* **206**, 1018 (2003).
- <sup>19</sup>S. Dhamodaran, A. P. Pathak, A. Dunlop, G. Jaskierowicz, and S. Della-Negra, *Nucl. Instr. Meth. B* **256**, 229 (2007).
- <sup>20</sup>A. Chettah, H. Kucal, Z. G. Wang, M. Kac, A. Meftah, and M. Toulemonde, *Nucl. Instr. Meth. B* **267**, 2719 (2009).

- <sup>21</sup>G. Fuchs, F. Studer, E. Balanzat, D. Groult, J. C. Jousset, and B. Raveau, *Nucl. Instr. Meth. B* **12**, 471 (1985).
- <sup>22</sup>C. Houpert, M. Hervieu, D. Groult, F. Studer, and M. Toulemonde, *Nucl. Instr. Meth. B* **32**, 393 (1988).
- <sup>23</sup>J. Vetter, *Rad. Meas.* **25**, 33 (1995).
- <sup>24</sup>J. Vetter, R. Scholz, D. Dobrev, and L. Nistor, *Nucl. Instr. Meth. B* **141**, 747 (1998).
- <sup>25</sup>J. Henry, A. Dunlop, and S. Della-Negra, *Nucl. Instr. Meth. B* **146**, 405 (1998).
- <sup>26</sup>F. Studer, M. Hervieu, J. M. Costantini, and M. Toulemonde, *Nucl. Instr. Meth. B* **122**, 449 (1997).
- <sup>27</sup>L. A. Bursill and G. Braunshausen, *Philos. Mag.* **62**, 395 (1990).
- <sup>28</sup>C. Houpert, F. Studer, D. Groult, and M. Toulemonde, *Nucl. Instr. Meth. B* **39**, 720 (1989).
- <sup>29</sup>M. Toulemonde, G. Fuchs, N. Nguyen, F. Studer, and D. Groult, *Phys. Rev. B* **35**, 6560 (1987).
- <sup>30</sup>M. Toulemonde, W. Assmann, C. Dufour, A. Meftah, F. Studer, and C. Trautmann, *Mat. Fys. Medd.* **52**, 263 (2006).
- <sup>31</sup>B. Canut, R. Brenier, A. Meftah, P. Moretti, S. Ould Salem, S. M. M. Ramos, P. Thévenard, and M. Toulemonde, *Nucl. Instr. Meth. B* **91**, 312 (1994).
- <sup>32</sup>C. Trautmann, M. Toulemonde, J. M. Costantini, J. J. Grob, and K. Schwartz, *Phys. Rev. B* **62**, 13 (2000).
- <sup>33</sup>C. Trautmann, M. Boccanfuso, A. Benyagoub, S. Klaumünzer, K. Schwartz, and M. Toulemonde, *Nucl. Instr. Meth. B* **191**, 144 (2002).
- <sup>34</sup>M. Boccanfuso, A. Benyagoub, K. Schwartz, M. Toulemonde, and C. Trautmann, *Prog. Nucl. Energ.* **38**, 271 (2001).
- <sup>35</sup>A. S. El-Said, M. Cranney, N. Ishikawa, A. Iwase, R. Neumann, K. Schwartz, M. Toulemonde, and C. Trautmann, *Nucl. Instr. Meth. B* **218**, 492 (2004).
- <sup>36</sup>F. Studer, N. Nguyen, G. Fuchs, and M. Toulemonde, *Hyperfine Interact.* **29**, 1287 (1986).
- <sup>37</sup>J. M. Costantini, J. L. Flament, L. Sinopoli, D. Groult, F. Studer, M. Toulemonde, J. Trochon, and J. L. Uzureau, *Rad. Eff. Def. Sol.* **110**, 193 (1989).
- <sup>38</sup>P. Thévenard, G. Guiraud, C. H. S. Dupuy, and B. Delaunay, *Rad. Eff.* **32**, 83 (1977).
- <sup>39</sup>G. Szenes, *Phys. Rev. B* **51**, 8026 (1995).
- <sup>40</sup>G. Szenes, *Phys. Rev. B* **54**, 12458 (1996).
- <sup>41</sup>G. Szenes, *Nucl. Instr. Meth. B* **166-167**, 949 (2000).

- <sup>42</sup>B. Canut, S. M. M. Ramos, R. Brenier, P. Thévenard, J. L. Loubet, and M. Toulemonde, *Nucl. Instr. Meth. B* **107**, 194 (1996).
- <sup>43</sup>F. Thibaudau, J. Cousty, E. Balanzat, and S. Bouffard, *Phys. Rev. Lett.* **67**, 1582 (1991).
- <sup>44</sup>S. Bouffard, J. Cousty, Y. Pennec, and F. Thibaudau, *Radiat. Eff. Def. Solids* **126**, 225 (1993).
- <sup>45</sup>J. Ackermann, N. Angert, R. Neumann, C. Trautmann, M. Dischner, T. Hagen, and M. Sedlacek, *Nucl. Instr. Meth. B* **107**, 181 (1996).
- <sup>46</sup>R. Neumann, *Nucl. Instr. Meth. B* **151**, 42 (1999).
- <sup>47</sup>D. D. N. Barlo Daya, A. Hallen, P. Hakansson, B. U. R. Sundqvist, and C. T. Reiman, *Nucl. Instr. Meth. B* **103**, 454 (1995).
- <sup>48</sup>M. Döbeli, F. Ames, C. R. Musil, L. Scandella, M. Suter, and H. Y. Synal, *Nucl. Instr. Meth. B* **143**, 503 (1998).
- <sup>49</sup>S. Bouffard, C. Leroy, S. Della-Negra, A. Brunelle, and J. M. Costantini, *Philos. Mag.* **81**, 2841 (2001).
- <sup>50</sup>D. Albrecht, P. Armbruster, R. Spohr, M. Roth, K. Schaupt, and H. Stuhmann, *Appl. Phys. A* **37**, 37 (1985).
- <sup>51</sup>V. Chailley, E. Dooryhee, S. Bouffard, E. Balanzat, and M. Levalois, *Nucl. Instr. Meth. B* **91**, 162 (1994).
- <sup>52</sup>A. Meftah, F. Brisard, J. M. Costantini, M. Hage-Ali, J. P. Stoquert, F. Studer, and M. Toulemonde, *Phys. Rev. B* **48**, 920 (1993).
- <sup>53</sup>M. Toulemonde and F. Studer, *Philos. Mag. A* **58**, 799 (1988).
- <sup>54</sup>A. Meftah, J. M. Costantini, N. Khalfaoui, S. Boudjadar, J. P. Stoquert, F. Studer, and M. Toulemonde, *Nucl. Instr. Meth. B* **237**, 563 (2005).
- <sup>55</sup>J. M. Costantini, F. Ravel, F. Brisard, M. Caput, and C. Cluzeau, *Nucl. Instr. Meth. B* **80-81**, 1249 (1993).
- <sup>56</sup>A. Meftah, F. Brisard, J. M. Costantini, E. Dooryhee, M. Hage-Ali, M. Hervieu, J. P. Stoquert, F. Studer, and M. Toulemonde, *Phys. Rev. B* **49**, 12457 (1994).
- <sup>57</sup>J. M. Costantini, F. Brisard, J. L. Flament, A. Meftah, M. Toulemonde, and M. Hage-Ali, *Nucl. Instr. Meth. B* **65**, 568 (1992).
- <sup>58</sup>J. Jensen, A. Dunlop, S. Della-Negra, and M. Toulemonde, *Nucl. Instr. Meth. B* **146**, 412 (1998).
- <sup>59</sup>M. Toulemonde, C. Dufour, A. Meftah, and E. Paumier, *Nucl. Instr. Meth. B* **166-167**, 903 (2000).
- <sup>60</sup>M. Toulemonde, W. Assmann, C. Trautmann, and F. Grüner, *Phys. Rev. Lett.* **88**, 057602 (2002).
- <sup>61</sup>H. M. Naguib and R. Kelly, *Radiat. Eff.* **25**, 1 (1975).
- <sup>62</sup>S. Hémon, F. Goubilleau, C. Dufour, E. Paumier, E. Dooryhee, and A. Rouanet, *Nucl. Instr. Meth. B* **122**, 526 (1997).
- <sup>63</sup>A. Berthelot, S. Hémon, F. Goubilleau, C. Dufour, E. Dooryhee, and E. Paumier, *Nucl. Instr. Meth. B* **146**, 437 (1998).
- <sup>64</sup>A. Berthelot, S. Hémon, F. Goubilleau, C. Dufour, B. Domenges, and E. Paumier, *Phil. Mag. A* **80**, 2257 (2000).
- <sup>65</sup>T. Wiss, H. Matzke, C. Trautmann, M. Toulemonde, and S. Klaumünzer, *Nucl. Instr. Meth. B* **122**, 583 (1997).
- <sup>66</sup>T. Sonoda, M. Kinoshita, N. Ishikawa, M. Sataka, A. Iwase, and K. Yasunaga, *Nucl. Instr. Meth. B* **268**, 3277 (2010).
- <sup>67</sup>S. Moll, L. Thomé, L. Vincent, F. Garrido, G. Sattouy, T. Thomé, J. Jagielski, and J. M. Costantini, *J. Appl. Phys.* **105**, 023512 (2009).
- <sup>68</sup>F. Garrido, S. Moll, G. Sattouy, L. Thomé, and L. Vincent, *Nucl. Instr. Meth. B* **267**, 1451 (2009).
- <sup>69</sup>M. Lang, J. Lian, J. Zhang, F. Zhang, W. J. Weber, C. Trautmann, and R. C. Ewing, *Phys. Rev. B* **79**, 224105 (2009).
- <sup>70</sup>K. Schwartz, C. Trautmann, T. Steckenreiter, O. Geiß, and M. Krämer, *Phys. Rev. B* **58**, 11232 (1998).
- <sup>71</sup>S. Abu Saleh and Y. Eyal, *J. Appl. Cryst.* **40**, S121 (2007).
- <sup>72</sup>N. Khalfaoui, C. C. Rotaru, S. Bouffard, M. Toulemonde, J. P. Stoquert, F. Haas, C. Trautmann, J. Jensen, and A. Dunlop, *Nucl. Instr. Meth. B* **240**, 819 (2005).
- <sup>73</sup>J. Jensen, A. Dunlop, and S. Della-Negra, *Nucl. Instr. Meth. B* **141**, 753 (1998).
- <sup>74</sup>S. Abu Saleh and Y. Eyal, *Philos. Mag.* **87**, 3697 (2007).
- <sup>75</sup>A. Benyagoub, F. Levesque, F. Couveur, C. Gilbert-Mougel, C. Dufour, and E. Paumier, *Appl. Phys. Lett.* **77**, 3197 (2000).
- <sup>76</sup>C. Gilbert-Mougel, F. Couveur, J. M. Costantini, S. Bouffard, F. Levesque, S. Hémon, E. Paumier, and C. Dufour, *J. Nucl. Mat.* **295**, 121 (2001).
- <sup>77</sup>A. Benyagoub, *Phys. Rev. B* **72**, 094114 (2005).
- <sup>78</sup>A. Benyagoub and F. Levesque, *Europhys. Lett.* **60**, 580 (2002).
- <sup>79</sup>S. Hémon, V. Chailley, E. Dooryhee, C. Dufour, F. Goubilleau, F. Levesque, and E. Paumier, *Nucl. Instr. Meth. B* **122**, 563 (1997).
- <sup>80</sup>T. Sonoda, M. Kinoshita, Y. Chimi, N. Ishikawa, M. Sataka, and A. Iwase, *Nucl. Instr. Meth. B* **250**, 114 (2006).
- <sup>81</sup>N. Ishikawa, Y. Chimi, O. Michikami, Y. Ohta, K. Ohhara, M. Lang, and R. Neumann, *Nucl. Instr. Meth. B* **266**, 3033 (2008).
- <sup>82</sup>H. Ohno, A. Iwase, D. Maturama, Y. Nishihata, J. Muzuki, N. Ishikawa, Y. Baba, N. Hirao, T. Sonoda, and M. Kinoshita, *Nucl. Instr. Meth. B* **266**, 2013 (2008).
- <sup>83</sup>C. Müller, K.-O. Voss, M. Lang, and R. Neumann, *Nucl. Instr. Meth. B* **212**, 318 (2003).
- <sup>84</sup>M. Boccanfuso, A. Benyagoub, K. Schwartz, C. Trautmann, and M. Toulemonde, *Nucl. Instr. Meth. B* **191**, 301 (2002).
- <sup>85</sup>M. Boccanfuso, A. Benyagoub, M. Toulemonde, C. Trautmann, K. Schwartz, and C. Dufour, *Nucl. Instr. Meth. B* **175-177**, 590 (2001).
- <sup>86</sup>C. Müller, M. Cranney, A. S. El-Said, N. Ishikawa, A. Iwase, M. Lang, and R. Neumann, *Nucl. Instr. Meth. B* **191**, 246 (2002).
- <sup>87</sup>C. R. Wie, T. Vrelland Jr., and T. A. Tombrello, *Nucl. Instr. Meth. B* **9**, 25 (1985).
- <sup>88</sup>R. Hellborg and G. Skog, *Phys. Scr.* **9**, 121 (1974).
- <sup>89</sup>J. Zhang, M. Lang, J. Lian, J. Liu, C. Trautmann, S. Della-Negra, M. Toulemonde, and R. C. Ewing, *J. Appl. Phys.* **105**, 113510 (2009).
- <sup>90</sup>M. Kumar, F. Singh, S. A. Khan, V. Baranwal, S. Kumar, D. C. Agarwal, A. M. Siddiqui, A. Tripathi, A. Gupta, D. K. Avasthi, and A. C. Pandey, *J. Phys. D* **38**, 637 (2005).
- <sup>91</sup>M. K. Patel, D. K. Avasthi, P. K. Kulriya, S. Kailas, J. C. Pivin, A. K. Tyagi, and V. Vijayakumar, *Nucl. Instr. Meth. B* **268**, 42 (2010).
- <sup>92</sup>G. Szenes, *Phys. Rev. B* **61**, 14267 (2000).
- <sup>93</sup>G. Szenes, *Phys. Rev. B* **52**, 6154 (1995).
- <sup>94</sup>J. F. Ziegler, J. P. Biersack, and U. Littmark, *The Stopping and Range of Ions in Solids* (Pergamon, New York, 1985).
- <sup>95</sup>M. Toulemonde, *Nucl. Instr. Meth. B* **250**, 263 (2006).
- <sup>96</sup>A. Kamarou, E. Wendler, and W. Wesch, *J. Appl. Phys.* **97**, 123532 (2005).
- <sup>97</sup>S. Bouffard, J. Dural, F. Levesque, and J. M. Ramillon, *Ann. Phys.* **14**, 395 (1998).
- <sup>98</sup>J. F. Ziegler, *Nucl. Instr. Meth. B* **219**, 1027 (2004).
- <sup>99</sup>S. Hémon, Ch. Dufour, F. Goubilleau, E. Paumier, E. Dooryhee, and S. Begin-Colin, *Nucl. Instr. Meth. B* **146**, 443 (1998).
- <sup>100</sup>A. Benyagoub, *Nucl. Instr. Meth. B* **225**, 80 (2004).
- <sup>101</sup>JCPDS (Joint Committee on Powder Diffraction Standards). For CaF<sub>2</sub>: JCPDS card No 1549.



- <sup>102</sup>I. Zizak, N. Darowski, S. Klaumünzer, G. Schumacher, J. W. Gerlach, and W. Assmann, *Nucl. Instr. Meth. B* **267**, 944 (2009).
- <sup>103</sup>H. P. Klug and L. E. Alexander, *X-ray Diffraction Procedures for Polycrystalline and Amorphous Materials* (Wiley, New York, 1974), p. 618.
- <sup>104</sup>J. P. Stoquert, F. Pécheux, Y. Hervé, H. Marchal, R. Stuck and P. Siffert, *Nucl. Instr. Meth. B* **136**, 1152 (1998).
- <sup>105</sup>C. Dufour, S. Hémon, F. Gourbilleau, E. Paumier, and E. Dooryhee, *Mater. Sci. Forum* **248**, 21 (1997).
- <sup>106</sup>C. Dufour, B. Leselier De Chezelles, V. Delignon, M. Toulemonde, and E. Paumier, in *Modification Induced by Irradiation in glasses*, edited by P. Mazzoldi (Elsevier, Amsterdam, 1992), p. 61.
- <sup>107</sup>M. P. R. Waligorski, R. N. Hamm, and R. Katz, *Nucl. Tracks Radiat. Meas.* **11**, 3 (1986).
- <sup>108</sup>R. F. Haglund and R. Kelly, *Mat. Fys. Medd.* **43**, 537 (1993).
- <sup>109</sup>N. Itoh and M. Stoneham, *Material Modifications by Electronic Excitations* (Cambridge Press University, United Kingdom, 2001).
- <sup>110</sup>M. Kumar, S. A. Khan, P. Rajput, F. Singh, A. Tripathi, D. K. Avasthi, and A. C. Pandey, *J. Appl. Phys.* **102**, 083510 (2007).
- <sup>111</sup>W. Assmann, M. Toulemonde, and C. Trautmann, *Top. Appl. Phys.* **110**, 401 (2007).
- <sup>112</sup>M. Toulemonde, C. Trautmann, E. Balanzat, K. Hjort, and A. Weidinger, *Nucl. Instr. Meth. B* **216**, 1 (2004).
- <sup>113</sup>C. Trautmann, M. Toulemonde, K. Schwartz, J. M. Costantini, and A. Müller, *Nucl. Instr. Meth. B* **164-165**, 365 (2000).
- <sup>114</sup>A. T. Davidson, K. Schwartz, J. D. Comins, A. G. Kozakiewicz, M. Toulemonde, and C. Trautmann, *Phys. Rev. B* **66**, 214102 (2002).
- <sup>115</sup>S. Abu Saleh and Y. Eyal, *Nucl. Instr. Meth. B* **230**, 246 (2005).
- <sup>116</sup>S. Abu Saleh and Y. Eyal, *Nucl. Instr. Meth. B* **209**, 113 (2003).
- <sup>117</sup>S. Schlutig, Ph.D. thesis, University of Caen, France, 2001 [<http://tel.archives-ouvertes.fr/tel-00002110/fr/>].
- <sup>118</sup>C. R. A. Catlow and A. M. Stoneham, *J. Phys. C* **16**, 4321 (1983).
- <sup>119</sup>P. Ruello, G. Petot-Ervas, C. Petot, and L. Desgranges, *J. Am. Ceram. Soc.* **88**, 604 (2005).
- <sup>120</sup>[<http://www.insc.anl.gov/matprop/uo2/>] (2003).
- <sup>121</sup>J. Schoenes, *Phys. Rep.* **63**, 301 (1980).
- <sup>122</sup>M. Huang, D. Schwen, and R. S. Averback, *J. Nucl. Mat.* **399**, 175 (2010).
- <sup>123</sup>J. P. Biersack and L. G. Haggmark, *Nucl. Instr. Meth.* **174**, 257 (1980).
- <sup>124</sup>P. Kluth, C. S. Schnohr, O. H. Pakarinen, F. Djurabekova, D. J. Sprouster, R. Giulian, M. C. Ridgway, A. P. Byrne, C. Trautmann, D. J. Cookson, K. Nordlund, and M. Toulemonde, *Phys. Rev. Lett.* **101**, 175503 (2008).
- <sup>125</sup>D. A. Young, *Nucl. Instr. Meth. B* **252**, 175 (2006).
- <sup>126</sup>D. Ashkenasi, H. Varel, A. Rosenfeld, F. Noack, and E. E. B. Campbell, *Nucl. Instr. Meth. B* **122**, 359 (1997).